Chaos

Exploiting circadian memory to hasten recovery from circadian misalignment

Cite as: Chaos **31**, 073130 (2021); https://doi.org/10.1063/5.0053441
Submitted: 07 April 2021 . Accepted: 23 June 2021 . Published Online: 14 July 2021

Talha Ahmed and Dan Wilson

Chaos ARTICLE scitation.org/journal/cha

Exploiting circadian memory to hasten recovery from circadian misalignment

Cite as: Chaos **31**, 073130 (2021); doi: 10.1063/5.0053441
Submitted: 7 April 2021 · Accepted: 23 June 2021 ·
Published Online: 14 July 2021

View Online Export Citation CrossMark

Talha Ahmed and Dan Wilson[a)]

AFFILIATIONS

Department of Electrical Engineering and Computer Science, University of Tennessee, Knoxville, Knoxville, Tennessee 37996, USA

[a)]**Author to whom correspondence should be addressed:** dwilso81@utk.edu

ABSTRACT

Recent years have seen a sustained interest in the development of circadian reentrainment strategies to limit the deleterious effects of jet lag. Due to the dynamical complexity of many circadian models, phase-based model reduction techniques are often an imperative first step in the analysis. However, amplitude coordinates that capture lingering effects (i.e., memory) from past inputs are often neglected. In this work, we focus on these amplitude coordinates using an operational phase and an isostable coordinate framework in the context of the development of jet-lag amelioration strategies. By accounting for the influence of circadian memory, we identify a latent phase shift that can prime one's circadian cycle to reentrain more rapidly to an expected time-zone shift. A subsequent optimal control problem is proposed that balances the trade-off between control effort and the resulting latent phase shift. Data-driven model identification techniques for the inference of necessary reduced order, phase-amplitude-based models are considered in situations where the underlying model equations are unknown, and numerical results are illustrated in both a simple planar model and in a coupled population of circadian oscillators.

Many practical jet-lag recovery strategies have been developed with knowledge of circadian phase response curves associated with various inputs. For instance, exposure to bright light before bedtime can delay the onset of sleep, while the same bright light tends to advance one's circadian phase when applied early in the morning. Comparatively little formal mathematical attention has been devoted to the study of circadian memory, for example, to understand how the history of applied inputs can have a lingering effect on circadian oscillations. In this work, we investigate the influence of circadian memory in the context of recovery from jet lag. In order to capture memory effects that are neglected by standard phase reduction approaches, we employ an operational phase and isostable coordinate based approach. Using this reduced order framework, we identify a latent phase shift that can prime circadian oscillations to recover more rapidly to an expected shift in environmental time and suggest an optimal control framework that can be used to efficiently manipulate the latent phase. This work provides compelling evidence that memory-based effects could have a profound influence on recovery from circadian misalignment and points to the need for a better understanding of circadian memory in living organisms.

I. INTRODUCTION

The master circadian pacemaker within the mammalian brain is comprised of roughly 20 000 coupled neurons located in the suprachiasmatic nucleus (SCN).[35,42] The collective oscillation that emerges in the SCN yields a robust endogenous circadian cycle with a near 24-h period. In normal circumstances, circadian rhythms can be readily entrained to daily time cues such as a 24-h light–dark cycle.[15,66] Jet lag is a form of circadian misalignment resulting from rapid travel across multiple time zones that is brought on by a mismatch between one's circadian phase and the associated environmental time.[2,45] Recent years have seen a sustained interest in the development of jet-lag mitigation strategies designed to accelerate reentrainment following rapid travel across multiple time zones. For instance, modeling studies have identified optimal schedules for rapidly acclimating to a new time zone through light avoidance and exposure;[3,13,47,67] some of these strategies have been implemented successfully in real-time using smartphone apps.[37]

Given the complexity and high dimensionality of many circadian models, phase-based model reduction is often a necessary first step in the analysis and identification of jet-lag mitigation strategies. From a mathematical perspective, many models used to study circadian physiology can be written as a set of differential equations of

the form

$$\dot{x} = F(x, p(t)), \tag{1}$$

where $x \in \mathbb{R}^N$ is the system state, F represents the nominal dynamics, and $p \in \mathbb{R}$ is a (potentially) time-varying parameter that can be used to incorporate features such as a 24-h light–dark cycle. When $p(t) = p_0$ where p_0 is some nominal, constant parameter, circadian models of the general form (1) usually admit a stable, T-periodic limit cycle $x^\gamma(t)$. Restricting attention to models of the form (1) that admit a stable limit cycle, one can define a phase, θ, by using the notion of isochrons[17,65] so that initial conditions with the same asymptotic convergence to the periodic orbit have the same phase. The phase dynamics can subsequently be analyzed in a phase reduced form,[26,51,65]

$$\dot{\theta} = \omega + Z_E(\theta)u(t), \tag{2}$$

where $Z_E(\theta) = \frac{\partial \theta}{\partial x} \cdot \frac{\partial F}{\partial p}$ is the effective phase response curve (PRC) with all partials evaluated at $x^\gamma(\theta(t))$ on the limit cycle and $u(t) = p(t) - p_0$ is an effective input. PRCs that capture the response to light and melatonin have been measured experimentally in humans.[8,23,30,32] Based on this information, practical jet-lag recovery treatments have been developed such as carefully timed combinations of light exposure and light avoidance,[9,53] evening ingestion of melatonin after eastward travel,[4,38,50] and combinations of both.[43] Other strategies for jet-lag prevention have been suggested, which seek to shift one's circadian rhythm pre-flight,[7,12,44] as would be useful when peak-level performance is necessary immediately in the new time zone (e.g., for professional athletes[46]).

Phase-only model reduction techniques of the form (2) are often employed to study circadian oscillations,[29,51,63] as well as relevant dynamical behaviors related to entrainment.[18,39,62,68] A significant limitation of the phase-only coordinate system is that it encodes for the asymptotic behavior of the unperturbed limit cycle oscillator. In applications where inputs are continuously applied (such as those that consider entrainment to an external input), the asymptotic phase does not always accurately reflect the state of the system; this issue becomes more pronounced when the externally applied input shifts the oscillator's state further from the underlying limit cycle. In order to alleviate these issues, information about amplitude dynamics, which can encode for memory-based effects, must be used to characterize how the system adapts in response to prior input. Indeed, these considerations are important when studying circadian oscillations. It is well-established that measured phase response curves to light depend on the history of light stimulation,[11,19,40,48,52] and preliminary evidence suggests that related memory-based effects could have a profound impact on jet-lag recovery. Furthermore, the authors of Ref. 1 found that desynchronizing the phases of neurons within the SCN greatly reduced the time required to recover from subsequent time shifts in the light schedule. In the context of the analysis of population-level oscillations of coupled circadian oscillators, reducing the phase cohesion through partial desynchronization can be thought of as a shift in the amplitude coordinate that indirectly influences oscillation timing (i.e., phase).

The primary purpose of this work is to investigate the influence of circadian memory (i.e., the notion that past inputs have a lingering effect on the dynamics) in the context of recovery from circadian misalignment. In order to capture memory effects that are neglected by the standard phase reduction (1), we employ an operational phase and isostable coordinate based approach suggested by Wilson and Ermentrout[60] in which phase is defined with respect to a distinct feature of a given limit cycle. Unlike reduction techniques that use an asymptotic definition of phase, to leading order, the operational phase dynamics depend on the amplitude coordinates allowing us to consider circadian memory. Using a calculus of variation framework, we explore a jet-lag pretreatment strategy that exploits circadian memory to prime one's circadian cycle to recover quickly in response to an anticipated time-zone shift. This strategy is fundamentally different than those suggested in Refs. 7, 12, and 44 (which exchange circadian misalignment in one's destination time zone for misalignment in one's home time zone). Additionally, we consider data-driven model identification techniques that could be employed to implement the proposed optimal control strategy in applications where the underlying model equations are unknown.

The organization of this paper is as follows: Section II provides necessary background on phase-amplitude coordinates and the operational phase and isostable coordinate framework. Section III highlights a motivating example of a situation where the isostable (amplitude) coordinates associated with a stable oscillation have a significant influence on reentrainment. Section IV formulates an optimal control strategy for shifting the isostable coordinates while leaving the operational phase coordinate unchanged to subsequently hasten recovery from circadian misalignment. This section also derives explicit, approximate solutions to the proposed optimal control problem that can be applied regardless of the dimension of the resulting operational phase-amplitude reduced order model. Section V illustrates the proposed control strategy on two different models, and Sec. VI provides concluding remarks.

II. BACKGROUND AND MOTIVATION FOR THE PROPOSED CONTROL FRAMEWORK

Given that many circadian models are both high-dimensional and nonlinear, phase-based model reduction is often a first step in their analysis. Below, we provide necessary background on the asymptotic phase, operational phase, and isostable reduction frameworks. Operational phase coordinates introduced in Ref. 60 encode for the timing of a distinct feature of the oscillation. Even when the state is far from the periodic orbit, these operational coordinates accurately reflect the timing of the chosen feature. By contrast, the asymptotic phase (defined by isochrons[17,65]) encodes for the asymptotic behavior of an oscillator. As such, it is not generally obvious how to interpret the phase for states that are far from the underlying periodic orbit. With this in mind, the notion of an operational phase will primarily be used to design and evaluate the jet-lag amelioration strategies presented in this work. Nevertheless, an understanding of the dynamical behavior of asymptotic phase coordinates will be useful in some of the mathematical derivations from Sec. IV. Additionally, the data-driven model identification strategy detailed in Appendix B and used in Sec. V only yields asymptotic phase and isostable coordinate reductions; direct relationships between operational and asymptotic phase reductions are discussed in Sec. II B.

A. Asymptotic phase and isostable reduction

A brief description of the asymptotic phase and isostable coordinate framework (cf. Refs. 49 and 59) is presented here. To begin, consider a general dynamical system of the form (1) with a T-periodic limit cycle $x^\gamma(t)$ that emerges taking $p(t) = p_0$. When $p(t)$ is held constant at this nominal value, one can define a phase $\theta \in [0, 2\pi)$ valid for all locations on the limit cycle and scaled so that $d\theta/dt = 2\pi/T = \omega$. One can define phase in the entire basin of attraction of the limit cycle using the notion of isochrons.[17,65] Isochrons are defined such that when $p(t) = p_0$, for any initial condition $a(0) \in x^\gamma(t)$, the isochron associated with $a(0)$ is defined to be the set of all $b(0)$ such that

$$\lim_{t\to\infty} ||a(t) - b(t)|| = 0, \tag{3}$$

where $||\cdot||$ can be any vector norm. The isochron-based definition of phase encodes for the infinite time behavior of solutions that have been perturbed from the limit cycle. In many situations, it is also useful to consider the amplitude dynamics that capture the transient decay of solutions toward the periodic orbit. In order to leverage Floquet theory,[22] one can first define $\Delta x(t) = x(t) - x^\gamma(t)$ so that to a linear approximation, the dynamics of Eq. (1) are

$$\Delta\dot{x} = J\Delta x, \tag{4}$$

where J is the time-varying Jacobian of F evaluated at both $x^\gamma(t)$ and $p = p_0$. Letting Φ be the fundamental matrix defined such that $\Delta x(T) = \Phi\Delta x(0)$, consider the eigenvalues and associated left and right eigenvectors of Φ denoted by λ_j, w_j, and v_j, respectively. Letting λ_1 be the nonunity eigenvalue (i.e., Floquet multiplier) of the largest magnitude, it is possible to define a set of isostable coordinates valid in the basin of attraction of the limit cycle according to[59]

$$\psi_1(x) = \lim_{k\to\infty}\left[w_1^T(\nu(t_\Gamma^k, x) - x_0)\exp(-\kappa_1 t_\Gamma^k)\right], \tag{5}$$

where t_Γ^k denotes time of the kth transversal of the $\theta = 0$ isochron, $\nu(t, x)$ gives the unperturbed flow of Eq. (1), x_0 is the intersection of the periodic orbit and the $\theta = 0$ isochron, and $\kappa_1 = \log(\lambda_1)/T$ is the associated Floquet exponent. Intuitively, the term $w_1^T(\nu(t_\Gamma^k, x) - x_0)$ captures the exponential decay toward the periodic orbit, and the term $\exp(-\kappa_1 t_\Gamma^k)$ grows at a corresponding rate. In the limit as time approaches infinity, the term inside the brackets of (5) converges to the isostable coordinate associated with the state x. In general, a collection of isostable coordinates can be defined for the N-dimensional system (1); however, it is not always possible to provide an explicit definition like the one from (5). Instead, one can define a collection of isostable coordinates $\psi_1, \ldots, \psi_{M-1}$ implicitly as level sets of Koopman eigenfunctions associated with the nonunity Floquet multipliers of the linearized dynamics. More details about the relationship of isostable coordinates to the Koopman operator can be found in Refs. 27 and 31. In the basin of attraction of the limit cycle, all isostable coordinates decay exponentially according to $\dot{\psi}_j = \kappa_j\psi_j$ in the absence of perturbation where $\kappa_j = \log(\lambda_j)/T$.

In the absence of other assumptions, the use of isochrons and isostable coordinates on its own does not yield any meaningful simplification of the system dynamics since the phase still depends on the state. However, by assuming that both $p(t) - p_0$ and $x - x^\gamma(t)$ are order ϵ term at all times where $0 < \epsilon \ll 1$, one can asymptotically expand Eq. (1) about $x^\gamma(t)$ to yield

$$\begin{aligned}\dot{x} &= F(x, p_0) + \frac{\partial F}{\partial p}(p(t) - p_0) + O(\epsilon^2)\\ &= F(x, p_0) + U(t) + O(\epsilon^2),\end{aligned} \tag{6}$$

where the partial derivative is evaluated at both $x^\gamma(t)$ and p_0 and $U(t) \in \mathbb{R}^N = \frac{\partial F}{\partial p}(p(t) - p_0)$. Changing to phase and isostable coordinates via the chain rule as in Refs. 59 and 64 gives

$$\dot{\theta} = \omega + Z(\theta)^T U(t) + O(\epsilon^2), \tag{7}$$

$$\begin{aligned}\dot{\psi}_j &= \kappa_j\psi_j + I_j(\theta)^T U(t) + O(\epsilon^2),\\ j &= 1, \ldots, N-1,\end{aligned} \tag{8}$$

where $Z(\theta)$ and $I_j(\theta)$ are the gradients of θ and ψ_j, respectively, taken with respect to the state x (i.e., the phase and isostable response curves). Numerical techniques based on the adjoint method of solution for computing these response curves are described in Refs. 5 and 64. It is often possible to ignore isostable coordinates ψ_j for which the corresponding Floquet exponents κ_j are large in magnitude so that they decay rapidly;[34,58,61] in this case, the resulting set of equations is of lower order than the original set of equations. Note that to leading order accuracy, the phase dynamics are uncoupled from the isostable dynamics; however, this is not generally true for higher order accuracy phase-amplitude reductions as explored and evaluated in detail in Refs. 55 and 59.

In this work, we will use a slightly different construction for the phase and isostable equations of the form (7) and (8),

$$\dot{\theta} = \omega + z(\theta)u(t), \tag{9}$$

$$\begin{aligned}\dot{\psi}_j &= \kappa_j\psi_j + i_j(\theta)u(t),\\ j &= 1, \ldots, N-1,\end{aligned} \tag{10}$$

where $z(\theta) \in \mathbb{R} = Z(\theta)^T\frac{\partial F}{\partial p}$, each $i_j(\theta) \in \mathbb{C} = I_j(\theta)^T\frac{\partial F}{\partial p}$, and $u(t) = p(t) - p_0$ with partial derivatives evaluated at x^γ and p_0. Note that $i_j(\theta)$ can generally take complex values, but this only happens when its associated Floquet exponent is complex-valued. If the Floquet exponents are real-valued, as is the case in the examples considered in this work, then each $i_j(\theta)$ will be real-valued. Considering the definition of $U(t)$ given directly below (6), one can verify that the phase and isostable dynamics from (9) and (10) are equivalent to those from (7) and (8).

B. Operational phase reduction

Defining phase in terms of the isochrons (3) encodes for asymptotic behavior, i.e., the oscillation timing after the state relaxes to the limit cycle. In many applications, however, including those that involve entrainment of circadian oscillators, external inputs are constantly applied and the state never reaches the limit cycle. In these cases, standard phase-amplitude reduction may not adequately capture the behavior of the full system. With this in mind, as in Ref. 60, an operational phase coordinate, $\theta^* \in [0, 2\pi)$, can be used that explicitly defines $\theta^* = 0$ to correspond to some feature of interest near the limit cycle. For example, $\theta^* = 0$ can be defined as

the time that a periodically spiking neuron fires an action potential, elevating its transmembrane voltage beyond its resting level. Intuitively, such a threshold can be represented as a Poincaré section,[54] with the time required to start at and return to $\theta^* = 0$ corresponding to the return time. When using operational phase coordinates, $\theta^* = 0$ can be distinctly measured on each cycle, even when the state is far from the periodic orbit. By contrast, the asymptotic phase, θ, can generally only be measured after an oscillator is allowed to relax to the limit cycle in the absence of any exogenous inputs.

The operational phase coordinate, $\theta^*(x)$, can be directly related to the phase and isostable coordinates from Eqs. (7) and (8). Following the construction from Ref. 60, let $x^\gamma(\theta)$ be a limit cycle where θ is the asymptotic phase. Letting x_k^γ and x_k be the kth element of $x^\gamma(\theta)$ and x, respectively, the $\theta^*(x) = 0$ level set can be defined as all states in the neighborhood of $x^\gamma(0)$ for which both $x_k = x_k^\gamma(0)$ and $\text{sign}\left(\frac{dx_k}{dt}|_x\right) = \text{sign}\left(\frac{dx_k}{dt}|_{x^\gamma(0)}\right)$. As discussed in Ref. 60, by leveraging the isostable coordinate framework, the definition of an operational phase can be extended to a neighborhood of the limit cycle. The subsequent operational phase and isostable coordinate dynamics of Eq. (6) are of the form

$$\begin{aligned} \dot{\theta}^* &= \omega + \sum_{j=1}^{N-1}(\alpha_j\psi_j) + Z^*(\theta^*)^T U(t) + O(\epsilon^2), \\ \dot{\psi}_i &= \kappa_i\psi_i + I_i^*(\theta^*)^T U(t) + O(\epsilon^2), \\ i &= 1,\ldots,N-1, \end{aligned} \tag{11}$$

where constants $\alpha_j \in \mathbb{C}$ characterize how $\dot{\theta}^*$ changes as the state is perturbed from the limit cycle and $Z^*(\theta^*)$ [respectively, $I^*(\theta^*)$] gives the gradient of the operational phase and isostable coordinate evaluated at θ^* on the limit cycle. Rewriting (11) in a similar form as (9) and (10) to emphasize the parameter perturbations yields

$$\begin{aligned} \dot{\theta}^* &= \omega + \sum_{j=1}^{N-1}(\alpha_j\psi_j) + z^*(\theta^*)u(t), \\ \dot{\psi}_i &= \kappa_i\psi_i + i_i^*(\theta^*)u(t), \\ i &= 1,\ldots,N-1, \end{aligned} \tag{12}$$

where $z^*(\theta^*) \in \mathbb{R} = Z^*(\theta^*)^T\frac{\partial F}{\partial p}$, each $i_j^*(\theta^*) \in \mathbb{C} = I_j^*(\theta^*)^T\frac{\partial F}{\partial p}$, and $u(t) = p(t) - p_0$ with partial derivatives evaluated at $x^\gamma(\theta)$ and p_0.

As shown in Ref. 60, the phase and isostable response curves from (11) are related to those from the phase-isostable reduced equations from (7) and (8) according to

$$\begin{aligned} Z^*(\theta^*) &= Z(\theta^*) + \sum_{j=1}^{N-1}\left(\frac{\alpha_j I_j(\theta^*)}{\kappa_j}\right), \\ I_i^*(\theta^*) &= I_i(\theta^*) \end{aligned} \tag{13}$$

for each $i = 1,\ldots,N-1$. Furthermore,

$$\alpha_i = \frac{\omega\kappa_j p_i^{x_k}(0)}{\dot{x}_k(0)} \tag{14}$$

for each $i = 1,\ldots,N-1$ where $p_j^{x_k}(0)$ is the kth element of the Floquet eigenfunction associated with ψ_i evaluated at $\theta = 0$ and $\dot{x}_k(0)$ is the time derivative of the kth component of x evaluated at $\theta = 0$ on the limit cycle. To leading order accuracy, an explicit relationship between the operational and asymptotic phase can also be obtained,

$$\theta = \theta^* - \sum_{j=1}^{N-1}\frac{\alpha_j\psi_j}{\kappa_j}. \tag{15}$$

III. MOTIVATION AND INTUITION FOR THE PROPOSED RAPID REENTRAINMENT STRATEGY

A. A motivating example illustrating the importance of amplitude coordinates when considering reentrainment

In order to illustrate the fundamental importance of amplitude coordinates in applications involving reentrainment, we consider a modified version of the radial isochron clock from Ref. 65,

$$\begin{aligned} \dot{x} &= \frac{2\pi}{T}\left[\sigma x(1-x^2-y^2) - y(1+\rho(x^2+y^2-1))\right] + f_e(t), \\ \dot{y} &= \frac{2\pi}{T}\left[\sigma y(1-x^2-y^2) + x(1+\rho(x^2+y^2-1))\right], \end{aligned} \tag{16}$$

where x and y are spatial coordinates and $f_e(t)$ is an entraining stimulus. When $f_e(t) = 0$ and $\rho > 0$, Eq. (16) has a stable limit cycle that traces out a unit circle with period T. The constant $\rho = 0.12$ determines how the radial distance from the periodic orbit influences the rate of revolution and $\sigma = 0.04$ sets the relaxation rate to the periodic orbit. For this specific example, we take $T = 24.2$ h and let $f_e(t) = 0.025\sin(2\pi t/24 + 0.58)$. These values are chosen to reflect the relationship between the free-running period of a circadian oscillator (slightly longer than 24 h[6,10]) and an exogenous 24-h signal (such as a light–dark cycle) to which the oscillator can entrain. Under the application of $f_e(t)$, all initial conditions converge to an entrained solution shown as a solid black line in panel (a) of Fig. 1. When the oscillator is entrained and $\text{mod}(t, 24) = 0$, $(x, y) = (1.12, 0)$ (green dot). Colored dots represent initial conditions on the entrained solution for which the external time has been shifted by Δt hours (e.g., as a result of a flight across one or more time zone). Open and closed circles correspond to positive and negative values of Δt, respectively. Subsequent reentrainment to the time-shifted stimulus is illustrated in panels (b) and (c). In general, reentrainment time increases as Δt becomes larger in magnitude.

Figure 1 illustrates how reentrainment time depends strongly on the magnitude of the time shift and corresponding misalignment in the angular direction. However, the radial direction also has a strong influence on reentrainment as can be seen in the colormap in panel (a) of Fig. 2. Panels (b) and (c) of Fig. 2 show corresponding simulations illustrating how the radial coordinate influences reentrainment: a larger radial coordinate results in more rapid reentrainment following a +6 h time shift, while the same increased radial coordinate delays reentrainment after a −6 h shift. This discrepancy exists despite the fact that each oscillator receives the same input $f_e(t)$ in each trial.

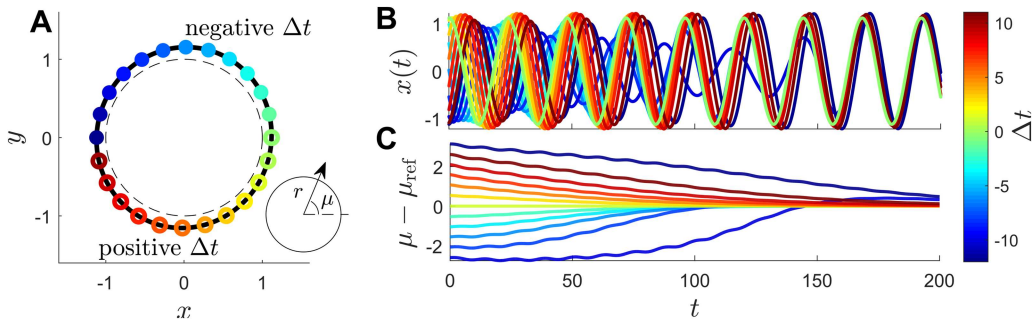

FIG. 1. In panel (a), the unperturbed periodic orbit [i.e., with $f_e(t) = 0$] is shown as a dashed line. Under the application of $f_e(t)$, the resulting fully entrained solution is shown in black. Colored dots represent initial conditions on the periodic orbit for which time [and the resulting perturbation $f_e(t)$] has suddenly been shifted to $\text{mod}(t, 24) = 0$, mimicking a time-zone change due to rapid travel. Open and closed circles represent initial conditions on the entrained solution, which have been shifted forward or backward in time, respectively. Panel (b) shows $x(t)$ during subsequent reentrainment for each initial condition. In panel (c), $\mu(t)$ is the angle in a radial coordinate system, and $\mu_{\text{ref}}(t)$ is the angle of the fully entrained solution.

B. Intuition behind the proposed pretreatment approach to hasten recovery from circadian misalignment

Intuition for the results shown in Fig. 2 can be gained by transforming the model (16) to polar coordinates using relationships $x = r\cos\mu$ and $y = r\sin(\mu)$, where r and μ represent a radial and angular coordinate, respectively. Using this coordinate transformation and momentarily letting $f_e(t) = 0$, one finds

$$\dot{\mu} = \frac{2\pi}{T}\left[1 + \rho(r^2 - 1)\right], \qquad \dot{r} = \frac{2\pi}{T}\left[\sigma(1 - r^2)r\right]. \tag{17}$$

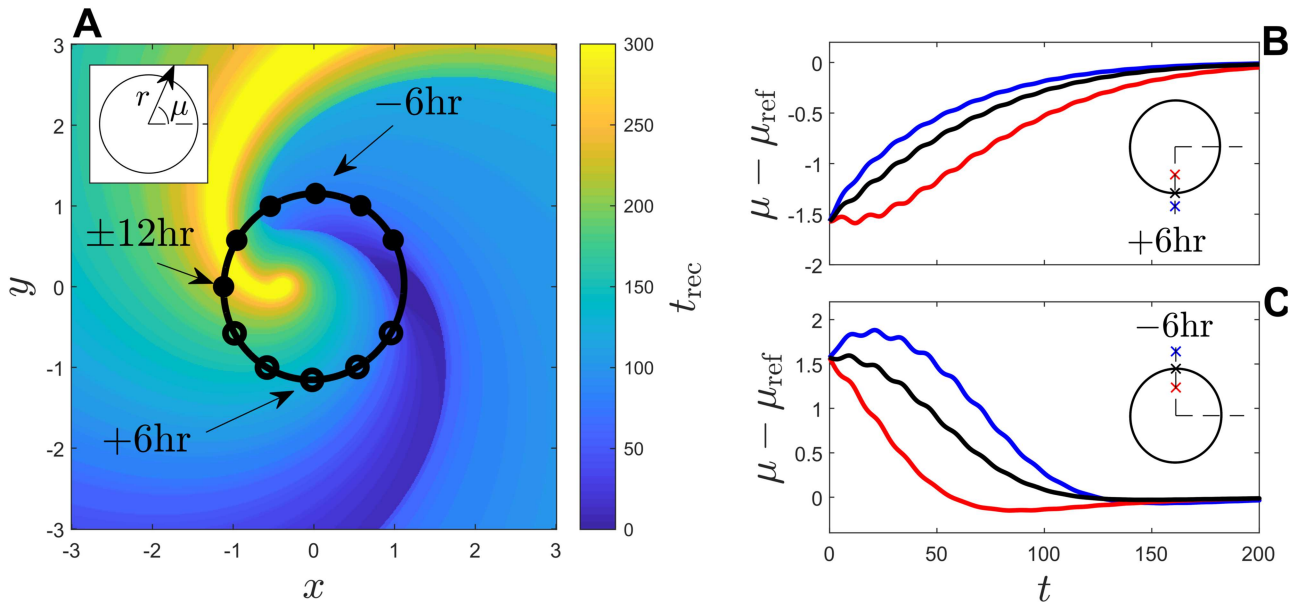

FIG. 2. Panel (a) shows the time for various initial conditions required to achieve entrainment to the input $f_e(t)$ starting at $t = 0$. In polar coordinates, taking $\mu_{\text{ref}}(t)$ to be the angular coordinate associated with the fully entrained solution, the recovery time t_{rec} is defined to be the largest t for which $|\mu(t) - \mu_{\text{ref}}(t)| > 0.26$, corresponding to a 1h time difference. Open and closed circles represent initial conditions on the entrained solution, which have been shifted forward or backward in time, respectively. Panel (b) [respectively, (c)] shows the recovery of initial conditions, which are initially $-\pi/2$ (respectively, $\pi/2$) radians out of phase due to a $+6$ (respectively, -6) h time shift. In each example, the radial direction significantly influences the recovery time.

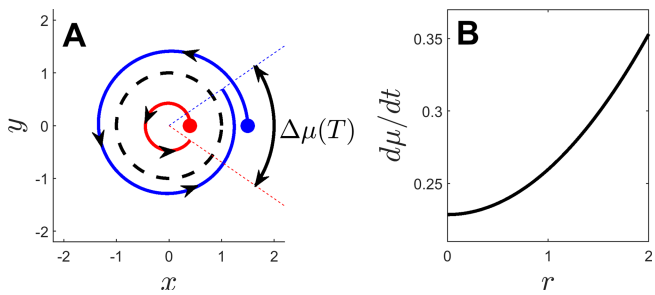

FIG. 3. Red and blue traces in panel (a) show two trajectories of Eq. (17), each starting at $\mu = 0$. The dashed line shows the nominal periodic orbit (with $r = 1$) for reference. After $T = 24.2$ time units have elapsed, the relative angular coordinates have substantially diverged. Panel (b) shows the time derivative of μ relative to the radial coordinate. For more complicated and higher dimensional models, the operational phase coordinate system described in Sec. II B can be used to quantify the change in the oscillation rate resulting from a shift in the amplitude coordinates. This strategy is used in the development of the jet-lag pretreatment strategy described in this work.

From this perspective, the angular rate of change grows monotonically with increasing r as shown in panel (b) of Fig. 3. Consequently, as highlighted in panel (a) of Fig. 3, initial conditions with larger radial coordinates will travel more rapidly than those with smaller radial coordinates. In the context of the results from Fig. 2, initial conditions with larger (respectively, smaller) radial coordinates are primed to recover more rapidly from positive (respectively, negative) time shifts to the entraining stimulus. Of course, the model (17) has very simple dynamics; more sophisticated analysis strategies are necessary to generalize this intuition when considering more complicated and higher dimensional dynamical models.

Motivated by the results above, in Secs. IV and V to follow, we propose and evaluate a jet-lag pretreatment strategy that seeks to optimally shift the amplitude coordinate in order to hasten circadian reentrainment following an expected time shift. This strategy uses the operational phase-isostable coordinate paradigm, which can be used to capture relationships between the amplitude coordinates and the rate of oscillation. This coordinate transformation can be generally applied to systems with stable limit cycles and is valid for and potentially high-dimensional models that are often used to characterize circadian oscillations. In contrast to many jet-lag recovery strategies that only consider the asymptotic phase dynamics of reduced order models, the use of the operational phase-amplitude coordinate framework allows us to exploit memory-based effects to achieve this goal.

IV. PROPOSED METHOD FOR OPTIMALLY SHIFTING AMPLITUDE COORDINATES

Here, we present an optimal control strategy for optimally shifting only the amplitude coordinates associated with a periodic orbit. As mentioned earlier, when larger magnitude amplitude coordinates are considered, the asymptotic phase from (9) does not, in general, accurately capture salient system behaviors. For this reason, we will employ the operational phase and isostable framework from Eq. (12).

A. Identifying an appropriate cost functional

Here, we pose an optimal control problem for a general model of the form (1) that can be represented in terms of its operational phase and isostable dynamics using a model of the form (12). In the derivation to follow, we assume that there are $\beta < N - 1$ non-truncated isostable coordinates yielding the reduced order model

$$\begin{aligned} \dot{\theta}^* &= \omega + \sum_{i=1}^{\beta} (\alpha_i \psi_i) + \epsilon z^*(\theta^*)(u(t) + u_e(t)), \\ \dot{\psi}_i &= \kappa_i \psi_i + \epsilon i_i^*(\theta^*)(u(t) + u_e(t)), \\ & i = 1, \ldots, \beta. \end{aligned} \tag{18}$$

Above, the overall input is comprised of the control input, $u(t)$, and a nominal entraining stimulus, $u_e(t)$ (for instance, a 24-h light–dark cycle). Above, it is explicitly assumed that the overall input is an order ϵ term where $0 < \epsilon \ll 1$. Furthermore, the entraining stimulus u_e is assumed to be T_e-periodic. Letting $\omega_e = 2\pi/T_e$, we also assume that $\omega - \omega_e$ is an order ϵ term, i.e., so that the entrained period is close to the natural period. Finally, as illustrated in Appendix C of Ref. 61, provided the input is an order ϵ term and sufficiently small relative to each Floquet exponent, each isostable coordinate is also an order ϵ term. Consider for the moment the stable, fully entrained solution of (18) that results in the limit as time approaches infinity when $u(t) = 0$. The associated operational phase and isostable dynamics on this fully entrained solution, $\theta_e^*(t)$ and $\psi_{i,e}(t)$, respectively, follow

$$\begin{aligned} \dot{\theta}_e^* &= \omega + \sum_{i=1}^{\beta} (\alpha_i \psi_{i,e}) + \epsilon u_e(t) z^*(\theta_e^*), \\ \dot{\psi}_{i,e} &= \kappa_i \psi_{i,e} + \epsilon i_i^*(\theta_e^*) u_e(t), \\ & i = 1, \ldots, \beta. \end{aligned} \tag{19}$$

To proceed, for any initial condition $\theta(0)^* = \theta_e^*$, letting $\Delta\theta^* = \theta^* - \theta_e^*$ and $\Delta\psi_i = \psi_i - \psi_{i,e}$, one finds

$$\begin{aligned} \Delta\dot{\theta}^* &= \dot{\theta}^* - \dot{\theta}_e^* \\ &= \sum_{i=1}^{\beta} \alpha_i \Delta\psi_i + \epsilon z^*(\theta^*) u(t) + \epsilon u_e(t)[z^*(\theta^*) - z^*(\theta_e^*)] + \mathcal{O}(\epsilon^2) \\ &= \sum_{i=1}^{\beta} \alpha_i \Delta\psi_i + \epsilon z^*(\theta^*) u(t) + \epsilon u_e(t) z^{*\prime}(\theta_e^*) \Delta\theta^* \\ &\quad + \mathcal{O}(\Delta\theta^{*2}) + \mathcal{O}(\epsilon^2), \end{aligned} \tag{20}$$

where $' \equiv \frac{d}{d\theta^*}$. Noticing that all terms of $\Delta\dot{\theta}^*$ are order ϵ terms, $\Delta\theta^*$ is an order ϵ term on $t \sim \mathcal{O}(1/\epsilon)$. As such, we can rewrite (20) as

$$\Delta\dot{\theta}^* = \sum_{i=1}^{\beta} \alpha_i \Delta\psi_i + \epsilon z^*(\theta^*) u(t) + \mathcal{O}(\epsilon^2). \tag{21}$$

In a similar manner, considering Eqs. (18) and (19), the dynamics of each isostable coordinate follow

$$\begin{aligned}\Delta\dot{\psi}_i &= \kappa_i\Delta\psi_i + \epsilon i_i^*(\theta^*)u(t) + \epsilon[i_i^*(\theta^*) - i_i^*(\theta_e^*)]u_e(t) + \mathcal{O}(\epsilon^2)\\ &= \kappa_i\Delta\psi_i + \epsilon i_i^*(\theta^*)u(t) + \epsilon u_e(t) i^{*\prime}(\theta_e^*)\Delta\theta^*\\ &\quad + \mathcal{O}(\Delta\theta^{*2}) + \mathcal{O}(\epsilon^2)\\ &= \kappa_i\Delta\psi_i + \epsilon i_i^*(\theta^*)u(t) + \mathcal{O}(\epsilon^2)\end{aligned} \tag{22}$$

for $i = 1, \ldots, \beta$.

Equations (21) and (22) will be used as a foundation in the following optimal control formulation. We consider an initial condition that is fully entrained to $u_e(t)$ at $t = 0$ with associated operational phase and isostable coordinates $\theta^*(0) = \Delta\theta^*(0) = 0$ and $\Delta\psi(0) = 0$. Suppose that at $t = T_e$ (i.e., after the entraining stimulus has been applied for one cycle), the external timing of the entraining stimulus suddenly shifts by Δt, more precisely,

$$u_e(t) = u_e(t + h(T_e)\Delta t), \tag{23}$$

where h is the unit step function. We seek some input $u(t)$ applied over $t \in [0, T_e]$ that will prime the system for recovery from the resulting misalignment by appropriately influencing the isostable coordinates. To this end, we consider all inputs $u(t)$ that yield $\Delta\theta^*(T_e) = 0$, in other words, the set of all inputs that have no net influence on the operational phase. Depending on whether Δt is positive or negative, we seek to find the stimulus that minimizes the cost functional

$$C = \begin{cases} \int_0^{T_e} X\epsilon^2 u^2(t)dt - (1-X)\sum_{i=1}^{\beta}\left(-\frac{\alpha_i\Delta\psi_i(T_e)}{\kappa_i}\right) & \text{if } \Delta t > 0,\\ \int_0^{T_e} X\epsilon^2 u^2(t)dt + (1-X)\sum_{i=1}^{\beta}\left(-\frac{\alpha_i\Delta\psi_i(T_e)}{\kappa_i}\right) & \text{if } \Delta t < 0.\end{cases} \tag{24}$$

Here, the term $\int_0^{T_e}\epsilon^2 u^2(t)dt$ is the L^2 norm of the input $\epsilon u(t)$, which gives a sense of the control effort. Terms of the form $-\frac{\alpha_j\Delta\psi_j(T_e)}{\kappa_j}$ appropriately reward a latent phase shift that can be used to hasten resynchronization. To see this, considering Eq. (22) to leading order ϵ, $\Delta\psi_j(t) = \Delta\psi_j(T_e)\exp(\kappa_j(t - T_e))$ in the absence of input. As such, the total operational phase shift once the state relaxes back to the limit cycle will be

$$\begin{aligned}\lim_{t\to\infty}\Delta\theta^*(t) &= \int_{T_e}^{\infty}\left[\sum_{i=1}^{\beta}\alpha_i\Delta\psi_i(T_e)\exp(\kappa_i(t - T_e))\right]dt\\ &= \sum_{i=1}^{\beta} -\frac{\alpha_i\Delta\psi_i(T_e)}{\kappa_i}.\end{aligned} \tag{25}$$

As such, shifting the isostable coordinates can prime the underlying system (1) to respond appropriately to an expected shift in the environmental time. For instance, taking $\Delta t > 0$, the overall cost is decreased when the latent phase is positive, ultimately hasten resynchronization. Finally, $X \in (0, 1]$ is a weighting term that sets the relative importance of minimizing energy vs shifting the isostable coordinate.

The latent phase shift from Eq. (25) provides a way to quantify the influence of the isostable (amplitude) coordinates on the recovery from a time shift, Δt. For a given isostable coordinate, the associated latent phase shift is proportional to α_i (which characterizes how $\dot{\theta}^*$ changes in response to an isostable shift) and inversely proportional to κ_i (which sets the decay rate of the isostable coordinate). The goal in minimizing the cost functional from Eq. (24) is to find an energy efficient stimulus that appropriately shifts the latent phase, thereby hastening resynchronization.

B. A calculus of variations approach for minimizing the cost functional

Following a calculus of variations approach,[25] the Hamiltonian function associated with the cost functional (24) is

$$\begin{aligned}H(y(t), u(t), p(t), t) &= X\epsilon^2 u^2(t) + \lambda_0\left[\sum_{i=1}^{\beta}(\alpha_i\Delta\psi_i) + \epsilon z^*(\theta^*)u(t)\right]\\ &\quad + \sum_{i=1}^{\beta}\lambda_i[\kappa_i\Delta\psi_i + \epsilon i_i^*(\theta^*)u(t)],\end{aligned} \tag{26}$$

where $y \equiv [\Delta\theta^*\Delta\psi_1, \ldots, \Delta\psi_\beta]^T$ and $p \equiv [\lambda_0, \ldots, \lambda_\beta]^T$ are Lagrange multipliers. The associated Euler–Lagrange equations are

$$\dot{y} = \frac{\partial H}{\partial p}, \tag{27}$$

$$\dot{p} = -\frac{\partial H}{\partial y}, \tag{28}$$

$$0 = \frac{\partial H}{\partial u}. \tag{29}$$

The evaluation of (27) yields the state equations (21) and (22). Evaluation of (28) yields

$$\begin{aligned}\dot{\lambda}_0 &= -\epsilon z^{*\prime}(\theta^*)u(t)\lambda_0 - \sum_{i=1}^{\beta}\left(\epsilon i_i^{*\prime}(\theta^*)u(t)\lambda_i\right),\\ \dot{\lambda}_i &= -\lambda_i\kappa_i - \alpha_i\lambda_0.\end{aligned} \tag{30}$$

Finally, evaluation of (29) yields

$$u(t) = \frac{-\lambda_0 z^*(\theta^*) - \sum_{i=1}^{\beta}\lambda_i i_i^*(\theta^*)}{2\epsilon X}. \tag{31}$$

Equations (21), (22), (30), and (31) comprise a set of $2(\beta + 1)$ Euler–Lagrange equations that must be satisfied along extremal solutions. $\beta + 2$ of the required boundary conditions, $\Delta\theta^*(0) = \Delta\theta^*(T_e) = \Delta\psi_1(0) = \cdots = \Delta\psi_\beta(0) = 0$, have already been specified by the problem formulation. Noting that the final states of the isostable coordinates $\Delta\psi_1(T_e), \ldots, \Delta\psi_\beta(T_e)$ are free, the remaining boundary conditions can be specified by requiring[25]

$$\left.\frac{\partial g}{\partial\Delta\psi_i}\right|_{t=T_e} - \lambda_i(T_e) = 0 \tag{32}$$

for $i = 1, \ldots, \beta$, where $g = -\text{sign}(\Delta t)(1 - X)\sum_{i=1}^{\beta}\left(-\frac{\alpha_i\Delta\psi_i}{\kappa_i}\right)$ is used to determine the endpoint cost from (24). Evaluating (32)

yields the remaining boundary conditions

$$\lambda_i(T_e) = \text{sign}(\Delta t)(1 - X)\frac{\alpha_i}{\kappa_i} \tag{33}$$

for $i = 1, \ldots, \beta$.

As a matter of practical implementation, obtaining a solution to the above system of Euler–Lagrange equations involves identifying a set of initial values for the Lagrange multipliers, $\lambda_0(0), \ldots, \lambda_\beta(0)$, that yield the required final conditions at time T_e under the evolution of the Euler–Lagrange equations (27)–(29). This can be accomplished by first noting that when $X = 1$ in the cost functional (24), that $u(t) = 0$ is the minimal solution with corresponding $\lambda_i(0) = 0$ for $i = 0, 1, \ldots, \beta$. Subsequently, X can be incrementally decreased, and the required Lagrange multipliers at each increment can be obtained using a Newton iteration until the extremal solution for the desired value of X is identified.

C. An explicit formulation of an approximate solution to the optimal control problem

The process of finding solutions of the Euler–Lagrange equations (27)–(29) with the required boundary conditions becomes unwieldy as the number of isostable coordinates, and hence the dimensions of the Euler–Lagrange equations, increases. Additionally, it can be difficult to know if the resulting extremal solutions represent globally optimal solutions or merely locally optimal solutions. Here, we provide an explicit strategy to compute an approximate solution that minimizes the cost functional (24) that is valid in the limit that the magnitude of the input is small.

To begin, noticing from (18) that one can write $\dot{\theta}^* = \omega + \mathcal{O}(\epsilon)$ and recalling that $\theta^*(0) = 0$, one finds

$$\theta^*(t) = \omega t + \mathcal{O}(\epsilon). \tag{34}$$

With this in mind, considering the leading order ϵ dynamics of each $\Delta\psi_i$, by first defining $r_i \equiv \Delta\psi_i(t)e^{-\kappa_i t}$ and substituting this into Eq. (22), one finds

$$\Delta\dot{\psi}_i = \dot{r}_i e^{\kappa_i t} + \kappa_i r_i e^{\kappa_i t} = \kappa_i r_i e^{\kappa_i t} + \epsilon i_i^*(\omega t)u(t). \tag{35}$$

Hence,

$$\begin{aligned} \dot{r}_i &= \epsilon e^{-\kappa_i t} i_i^*(\omega t)u(t), \\ r_i(t) &= r(t_0) + \epsilon \int_0^t e^{-\kappa s} i_i^*(\omega s)u(s)ds. \end{aligned} \tag{36}$$

Substituting $\Delta\psi_i = r_i e^{\kappa_i t}$ into the above equation and recalling that $\Delta\psi_i(0) = 0$ yields

$$\Delta\psi_i(T_e) = \epsilon \int_0^{T_e} e^{\kappa_i(T_e - s)} i_i^*(\omega s)u(s)ds. \tag{37}$$

Substituting the above result into the cost functional from (24) gives

$$\begin{aligned} C = \int_0^{T_e} \Big[& X\epsilon^2 u^2(t) - \epsilon\,\text{sign}(\Delta t)(1 - X) \\ & \times \sum_{i=1}^{\beta} \left(-\frac{\alpha_i}{\kappa_i} e^{\kappa_i(T_e - t)} i_i^*(\omega t)u(t) \right) \Big] dt. \end{aligned} \tag{38}$$

The goal of the optimization is to find the input $u(t)$ that minimizes (38) subject to the constraint $\Delta\theta^*(T_e) = 0$. This constraint can be written in a form similar to (38) by considering the asymptotic phase dynamics using an equation of the form (9)

$$\dot{\theta} = \omega + \epsilon z(\theta)(u(t) + u_e(t)), \tag{39}$$

as well as the asymptotic phase dynamics of the fully entrained solution $\theta_e(t)$, which follows

$$\dot{\theta} = \omega + \epsilon z(\theta_e)u_e(t). \tag{40}$$

We will define $\Delta\theta \equiv \theta - \theta_e$. We also note $\theta = \theta^* + \mathcal{O}(\epsilon)$. Using a similar asymptotic expansion used to obtain (21), one can show

$$\Delta\dot{\theta} = \epsilon z(\omega t)u(t) + \mathcal{O}(\epsilon^2). \tag{41}$$

Noting that at $t = 0$, the system is fully entrained so that $\Delta\theta(0) = 0$, direct integration of (41) yields

$$\Delta\theta(T_e) = \int_0^{T_e} \epsilon z(\omega t)u(t)dt. \tag{42}$$

Applying (15), one can show that $\Delta\theta = \Delta\theta^* - \sum_{i=1}^{\beta}(\alpha_i \Delta\psi_i/\kappa_i)$. Using this result to transform (42) to operational phase coordinates, the required constraint for the cost functional optimization becomes

$$\begin{aligned} \Delta\theta^*(T_e) = 0 &= \int_0^{T_e} \epsilon z(\omega t)u(t)dt + \sum_{i=1}^{\beta} \frac{\alpha_i \Delta\psi_i(T_e)}{\kappa_i} \\ &= \epsilon \int_0^{T_e} \left[z(\omega t)u(t) + \sum_{i=1}^{\beta} \left(\frac{\alpha_i}{\kappa_i} e^{\kappa_i(T_e - t)} i_i^*(\omega t)u(t) \right) \right] dt, \end{aligned} \tag{43}$$

where the second line is obtained by substituting the result from (37). Using an optimization approach based on a calculus of variations formulation,[25] the integral constraint (43) can be rewritten as an ordinary differential equation

$$\frac{dQ}{dt} = \epsilon z(\omega t)u(t) + \epsilon \sum_{i=1}^{\beta} \left(\frac{\alpha_i}{\kappa_i} e^{\kappa_i(T_e - t)} i_i^*(\omega t)u(t) \right), \tag{44}$$

with boundary conditions $Q(0) = Q(T_e) = 0$. As such, the Hamiltonian associated with the cost functional (38) subject to the constraint from Eq. (44) is

$$\begin{aligned} H(y, u(t), p, t) = {} & X\epsilon^2 u^2(t) - \epsilon\,\text{sign}(\Delta t)(1 - X) \\ & \times \sum_{i=1}^{\beta} \left(-\frac{\alpha_i}{\kappa_i} e^{\kappa_i(T_e - t)} i_i^*(\omega t)u(t) \right) \\ & + \lambda_1 [\epsilon z(\omega t)u(t) + \epsilon \sum_{i=1}^{\beta} \left(\frac{\alpha_i}{\kappa_i} e^{\kappa_i(T_e - t)} i_i^*(\omega t) \right) u(t)], \end{aligned} \tag{45}$$

where $y = Q$ is the state and $p = \lambda_1$ is a single Lagrange multiplier. The Euler–Lagrange equations (27)–(29) once again can be used to

identify extremal solutions. Evaluation of (29) yields the input

$$u(t) = \frac{1}{2X\epsilon}\left(\text{sign}(\Delta t)(1-X)\sum_{i=1}^{\beta}\left(-\frac{\alpha_i}{\kappa_i}e^{\kappa_i(T_e-t)}i_i^*(\omega t)\right) - \lambda_1\left[z(\omega t) + \sum_{i=1}^{\beta}\left(\frac{\alpha_i}{\kappa_i}e^{\kappa_i(T_e-t)}i_i^*(\omega t)\right)\right]\right) = \lambda_1 u_\lambda(t) + u_0(t), \tag{46}$$

where $u_\lambda(t)$ and $u_0(t)$ are defined appropriately and are simply functions associated with the operational and asymptotic phase reduced equations. Note that $z(\omega t)$ in the above equation is the asymptotic phase response curve and not the operational phase response curve. Continuing to consider the Euler–Lagrange equations for (45), evaluation of Eq. (27) returns (44) and evaluation of (28) yields

$$\dot{\lambda}_1 = 0. \tag{47}$$

As such, λ_1 is a constant. With this information, substituting (46) into the constraint (43) gives

$$0 = \epsilon\int_0^{T_e}\left[\left(z(\omega t) + \sum_{i=1}^{\beta}\left(\frac{\alpha_i}{\kappa_i}e^{\kappa_i(T_e-t)}i_i^*(\omega t)\right)\right)(u_\lambda(t)\lambda_1 + u_0(t))\right]dt = \lambda_1 c_\lambda + c_0, \tag{48}$$

where $c_\lambda = \epsilon\int_0^{T_e}\left(z(\omega t) + \sum_{i=1}^{\beta}\left(\frac{\alpha_i}{\kappa_i}e^{\kappa_i(T_e-t)}i_i^*(\omega t)\right)\right)u_\lambda(t)dt$ and $c_0 = \epsilon\int_0^{T_e}\left(z(\omega t) + \sum_{i=1}^{\beta}\left(\frac{\alpha_i}{\kappa_i}e^{\kappa_i(T_e-t)}i_i^*(\omega t)\right)\right)u_0(t)dt$ are both constants. Provided $c_\lambda \neq 0$, the unique choice of λ_1 that satisfies the boundary conditions is

$$\lambda_1 = -c_0/c_\lambda, \tag{49}$$

and thus, an explicit approximation of the control input that minimizes the cost functional is

$$u(t) = -\frac{c_0}{c_\lambda}u_\lambda(t) + u_0(t), \tag{50}$$

which is valid in the limit that the magnitude of the input is small.

V. RESULTS

A. Illustration for a two-dimensional model

Here, we illustrate our proposed optimal control strategy on the nonradial isochron clock model from (16),

$$\begin{aligned}\dot{x} &= \frac{2\pi}{T}\left[\sigma x(1-x^2-y^2) - y(1+\rho(x^2+y^2-1))\right] \\ &\quad + f_e(t+h(T_e)\Delta t) + u(t) + \sqrt{2D}\eta(t), \\ \dot{y} &= \frac{2\pi}{T}\left[\sigma y(1-x^2-y^2) + x(1+\rho(x^2+y^2-1))\right].\end{aligned} \tag{51}$$

Equation (51) is identical to (16) except for the addition of the control input $u(t)$ and an independent and identically distributed, zero-mean white noise process $\sqrt{2D}\eta(t)$ with intensity D. As in Eq. (16), we take $f_e(t) = 0.025\sin(2\pi t/24 + 0.58)$. In this example, the term $h(T_e)$ is the unit step function that switches at time T_e and is used to model sudden time shifts in the light–dark cycle to mimic rapid travel across Δt time zones. All other constants and functions of (51) are taken to be the same as those from (16). For the

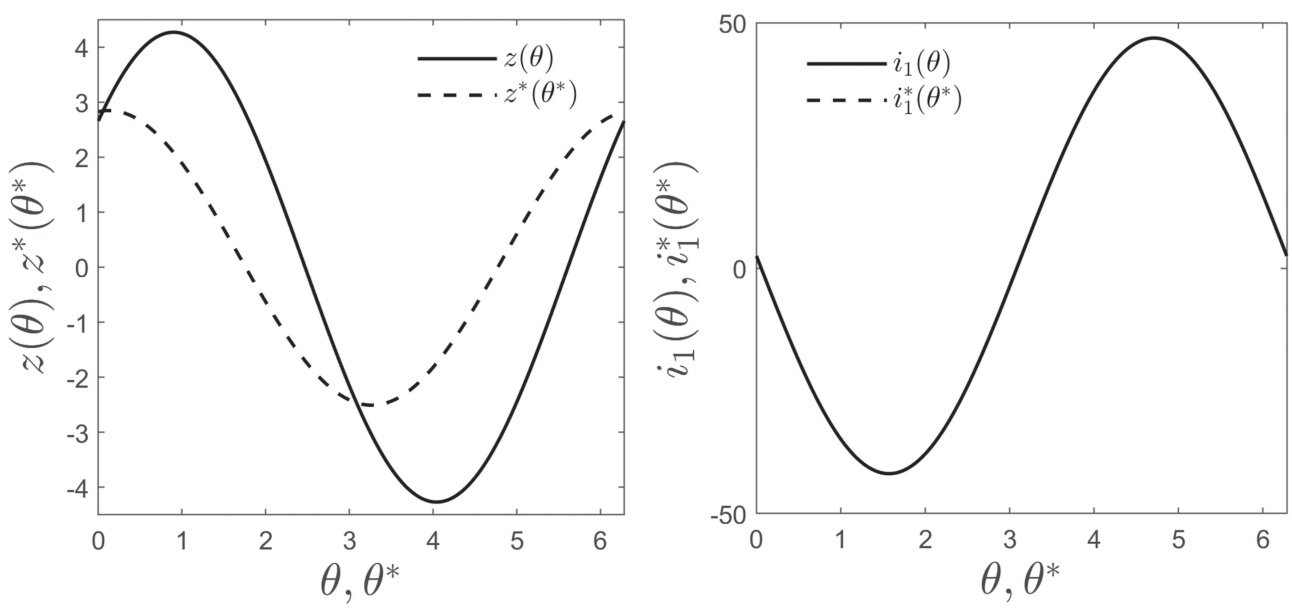

FIG. 4. For the periodic orbit that results when $f_e(t) = 0$ in (51), solid lines in the left and right panels show the asymptotic phase and isostable response curves, respectively, associated with input $u(t)$. Corresponding operational phase and isostable response curves are plotted with dashed lines. Note that $i_1(\theta)$ and $i_1^*(\theta^*)$ are identical.

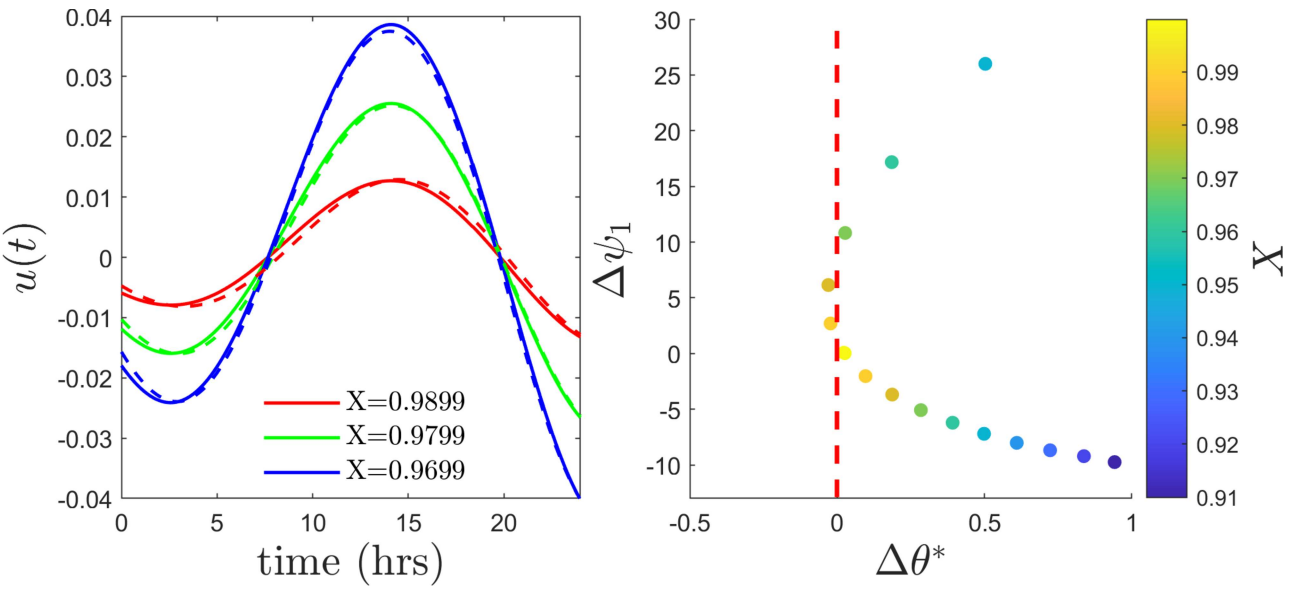

FIG. 5. When considering the nonradial isochron clock model from (51), optimal control inputs that minimize the cost functional (24) using negative values of Δt are obtained using the calculus of variations approach (solid lines) and shown in the left panel for various choices of X ranging from 0.91 to 0.9999. Note here that the sign of Δt sets the form of the cost functional from Eq. (24), which ultimately determines the sign of the target isostable coordinate. Approximations of the optimal inputs computed according to Eq. (50) are shown as dashed lines. The right panel shows resulting values of $\Delta\psi_1$ and $\Delta\theta^*$ when optimal inputs obtained for both positive and negative values of Δt are applied to the full model equations (51). The dashed red line shows the target value of $\Delta\theta = 0$. The proposed method yields results that are close to this target value when the input magnitudes are small. This effectiveness is degraded for smaller values of X, which yield larger magnitude inputs. In the right panel, the resulting optimal stimuli are being evaluated with respect to their ability to satisfy the constraints of the optimal control problem, i.e., to shift the isostable coordinate without yielding a net change in the operational phase. Resulting recovery times for specific time shifts are illustrated in Fig. 6.

moment, we will consider $D = 0$ (we will consider the influence of noise momentarily). As demonstrated in Fig. 2, the time required for reentrainment is directly related to the isostable (amplitude) coordinate directly before the external time shift. By implementing the control strategies from Sec. IV, it is possible to hasten recovery by applying a control designed to appropriately shift the isostable coordinate.

Toward obtaining the model dynamics in terms of phase and isostable coordinates, for the moment taking $f_e(t) = u(t) = 0$, the resulting periodic orbit has a period of $T = 24.2\,\mathrm{h}$ with a single nonunity Floquet multiplier $\lambda_1 = 0.605$ with the corresponding Floquet exponent $\kappa_1 = -0.021$. The adjoint method[5,64] is used to compute the asymptotic phase and isostable response curves for the transformation to phase and isostable coordinates (9) and (10). In this example, we consider $u(t)$ to be the adjustable parameter with $u(t) = 0$ being the nominal value. When considering operational phase and isostable coordinates of this system, we define the $\theta^* = 0$ level set to correspond to when $x(t)$ crosses 0 with a positive slope. With this definition of $\theta^* = 0$, $\alpha_1 = -0.0014$, computed according to Eq. (14), it indicates that increasing the isostable coordinate will slow down the nominal rate of oscillation. The subsequent operational phase response curves are computed from the asymptotic response curves using the relations given in (13). Figure 4 shows the corresponding operational and asymptotic phase and isostable response curves.

The resulting operational phase and isostable reduced coordinate framework is used in conjunction with the optimal control strategy from Sec. IV. The calculus of variations approach is applied to minimize the cost functional (24) with resulting optimal inputs shown as solid lines in the left panel of Fig. 5 for various values of X and negative values of Δt. Each input is designed to begin when $\mathrm{mod}(t, 24) = 0$ for an initial condition that is fully entrained to the external input $f_e(t)$ and end 24 h later, i.e., before a time shift at $T_e = 24\,\mathrm{h}$. The approximate control input that minimizes the cost functional (50) is also shown using dashed lines of corresponding color. The resulting approximate optimal inputs and the inputs obtained from the solution of the Euler–Lagrange equations are nearly identical.

Resulting optimal inputs are applied to the full model equations (51) in order to assess their effectiveness. Starting from a fully entrained solution at $t = 0$, inputs are applied on the interval $t = [0, 24]$, and the resulting isostable and operational phase coordinates are compared to $\theta_e^*(24)$ and $\psi_e(24)$, i.e., the values on the entrained solution; resulting differences are shown in the right panel of Fig. 5. For values of X near 1, the resulting optimal inputs yield values of $\Delta\theta^*$ that are close to zero as desired. For large magnitude inputs that result when taking smaller values of X, the validity of the operational reduction starts to degrade due to nonlinear terms that are unaccounted for in the equations for the phase and isostable dynamics. This subsequently yields larger (undesired) shifts in the

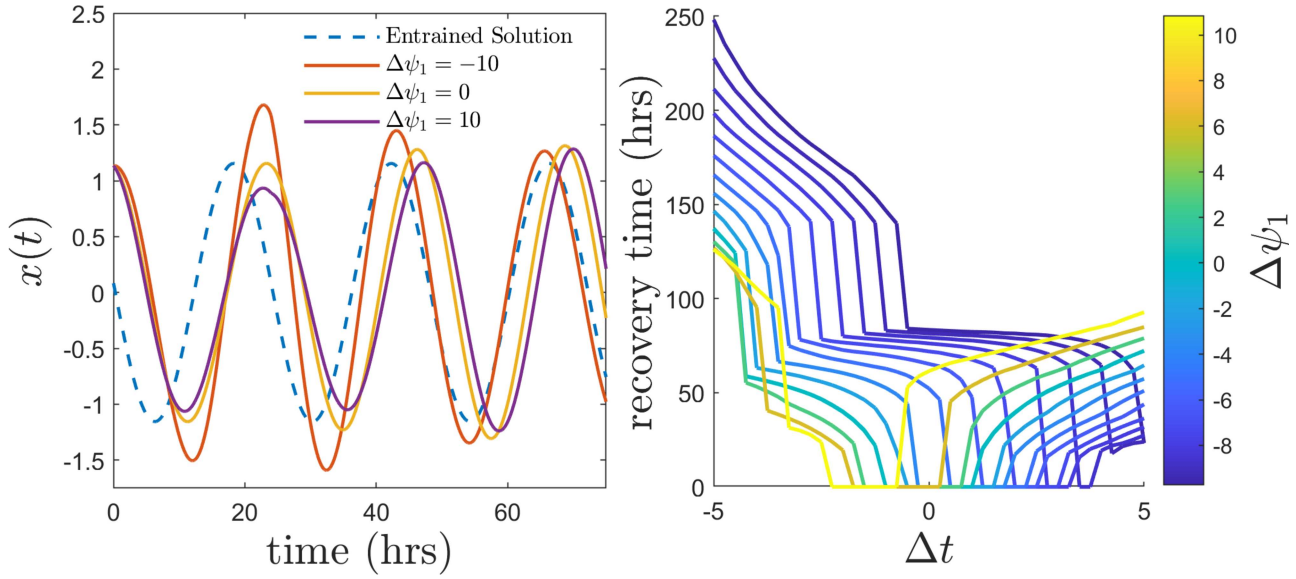

FIG. 6. The optimal control strategy is designed to shift the isostable coordinates while leaving the operational phase coordinates unchanged. As seen in the right panel, inputs that shift the isostable coordinates to more positive (respectively, negative) values decrease the recovery times in response to negative (respectively, positive) time shifts. The left panel illustrates the recovery to a time shift of $\Delta t = +5$ h occurring at $T_e = 24$ following the application of three different inputs applied on $t \in [0, 24]$ that yield different values of $\Delta\psi_1(24)$. For reference, the dashed blue line shows a solution that is fully entrained in the shifted time zone.

value of $\Delta\theta^*$. As such, only inputs that yield results with $|\Delta\psi| < 10$ will be considered further.

Finally, we investigate the recovery times of the resulting optimal stimuli with results shown in Fig. 6. In order to measure the recovery times following a given time shift, the system (51) is first simulated with $u(t) = 0$ until it is fully entrained to $f_e(t)$. For choices of X ranging from 0.91 to 0.9999, corresponding optimal stimuli are computed and applied over a 24-h period to produce an associated shift in the isostable coordinate, $\Delta\psi_1$. Immediately after the conclusion of the application of the optimal stimulus, at $T_e = 24$ h, the external time is shifted by some amount Δt, representing rapid travel through multiple time zones. The subsequent recovery time is taken to be the amount of time required for θ^* to return to within 1 h of the fully entrained solution. The right panel of Fig. 6 shows the resulting recovery times. For the curve corresponding to $\Delta\psi_1 = 0$, i.e., that results when $u(t) = 0$, there is a 2-h window centered at $\Delta t = 0$ within which the recovery time is zero since, by definition, the time shift is so small that recovery happens immediately. By applying an optimal input before the external time shift occurs, this window is shifted in response to the shifted isostable coordinate. Positive (respectively, negative) shifts in the isostable coordinate yield more rapid recoveries for negative (respectively, positive) shifts in time. The left panel of Fig. 6 shows the recovery in response to a time shift of $\Delta t = +5$ h illustrating that by first applying a stimulus that yields a decrease in the isostable coordinate, subsequent recovery is hastened.

B. Implementation of the proposed control strategy using data-driven techniques to infer the reduced order models

In Sec. V A, we consider a noiseless version of (51) and assume that the phase and isostable response curves can be computed directly with knowledge of the underlying model equations (using the adjoint method). Here, we relax these assumptions to illustrate that the proposed control strategy can be implemented in noisy environments when the underlying model equations are unknown. To proceed, we will take $\sqrt{2D} = 0.0032$ to be the noise strength and implement the data-driven model inference strategy previously developed in Ref. 57 and summarized in Appendix B.

Following Steps 1–6 from Appendix B, we assume that we can take direct measurements of $x(t)$ from the noisy model (51) and define $\theta^* = 0$ to correspond to when $x(t)$ crosses 0 with a positive slope. The nominal period is estimated to be $T = 24.2$ h by taking the average time between subsequent crossings of the $\theta^* = 0$ threshold. Following Step 2, using a sampling rate of $\Delta t = 0.04$ h, 300 separate oscillations measured over one period are shown in panel (a) of Fig. 7, the average value γ is shown as a black line, and values of $x(t) - \gamma(t)$ that comprise the matrix B from Eq. (B2) are shown in panel (b). As part of Step 3, POD modes are obtained and shown in panel (c). Only $m = 2$ POD modes are required here, with $\sum_{j=1}^{2} \zeta_j / \sum_{j=1}^{\alpha} \zeta_j = 0.99$. Consequently, the dynamics of this system can be captured with one phase coordinate and one isostable coordinate. Step 4 is implemented to obtain the update matrix A_M as

part of Eq. (B4). The resulting matrix A_M has eigenvalues $\lambda_1 = 0.74$ (corresponding to the decay of the isostable coordinate) and $\lambda_2 = 1$ (associated with the phase dynamics). Steps 5 and 6 are performed to yield a direct method estimate of the phase and isostable response curves. For each trial of the direct method, after initial transients are allowed to decay, a perturbation of magnitude 0.1 is applied for 2 h, and the subsequent recovery is used in conjunction with Eqs. (B5) and (B6) to obtain the resulting shift in the isostable and phase coordinate. This information is used to obtain estimates of the isostable and phase response curves as described in Step 6. Black dots in panels (d) and (e) of Fig. 7 show the results of each trial from the implementation of the direct method, and the resulting data points are fit to a sinusoidal basis $z(\theta) = b_0^z + a_1^z \sin(\theta) + b_1^z \cos(\theta)$ and $i_1(\theta) = b_0^i + a_1^i \sin(\theta) + b_1^i \cos(\theta)$ with coefficients chosen to minimize the sum of the squared residuals. For reference, dashed lines show the phase and isostable response curves from Fig. 4 obtained from the adjoint method. Using Eq. (13), the operational response curves are computed and shown in panels (f) and (g). As part of this computation, α_1 is found using (14), where $\dot{x}_k(0)$ is the time derivative of γ evaluated at $\theta = 0$ and $p_1^x(0)$ is taken to be the first component of Φv_1. Here, v_1 is the eigenvector of A_M associated with the eigenvalue $\lambda_1 = 0.74$; as such, Φv_1 corresponds to p_1^x as required by (14). Notice from panels (d)–(e) of Fig. 7, the reduced order curves obtained using the adjoint method are nearly identical to those obtained from the direct method.

Similar to the results shown in Fig. 5, optimal inputs that minimize the cost functional (24) are obtained using the calculus of variations approach detailed in Sec. IV B. Resulting optimal inputs are shown as solid lines in Fig. 8 for various values of the weighting parameter X when taking a negative value for Δt. For comparison, dashed lines show nearly identical optimal inputs (from Fig. 5) that result when using the true reduced order equations obtained directly from the full model. When these inputs are applied to the full model, shifts in recovery times are nearly identical to those shown in the right panel of Fig. 6 (results not shown).

C. Illustration for a large model of coupled circadian oscillators

Mammalian circadian rhythms in humans are governed by the suprachiasmatic nucleus (SCN), a master pacemaker comprised of approximately 20 000 coupled neurons.[35,42] Here, we consider a

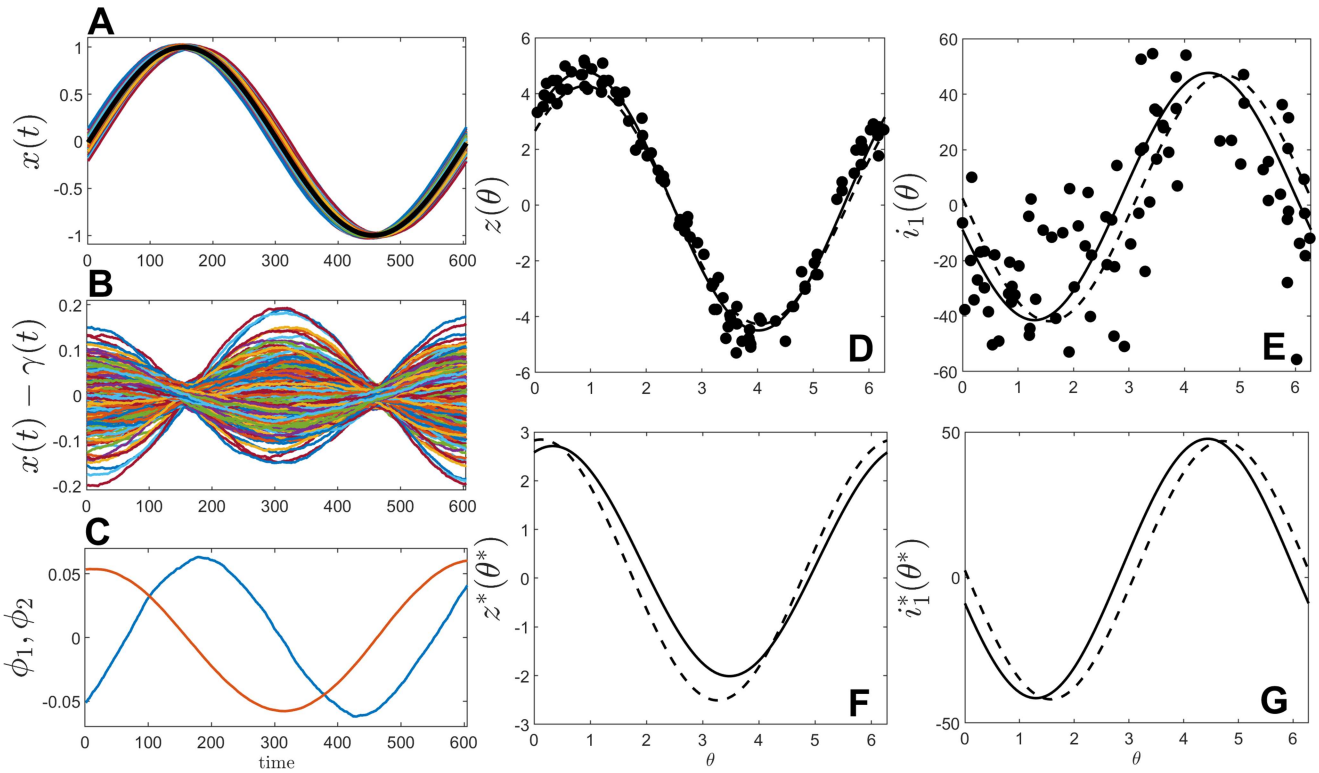

FIG. 7. Illustration of the data-driven model inference strategy for the nonradial isochron clock model (51). Colored lines in panel (a) show $x(t)$ sampled over 300 noisy cycles. The black line, which is the average of these cycles, is taken to be the periodic orbit, γ. Panel (b) shows values of $x - \gamma$, POD is performed on the data, and two POD modes are sufficient to represent this data. A direct method strategy described in Step 6 of Appendix B is performed, with individual measurements shown as black dots in panels (d) and (e). Solid black lines are obtained by fitting the data to a sinusoidal basis. This information is used to calculate the terms of the operational phase and isostable reduction, with results shown in panels (f) and (g). Dashed lines in panels (d)–(g) show exact values of the corresponding curves (as shown in Fig. 4) computed using the adjoint method.

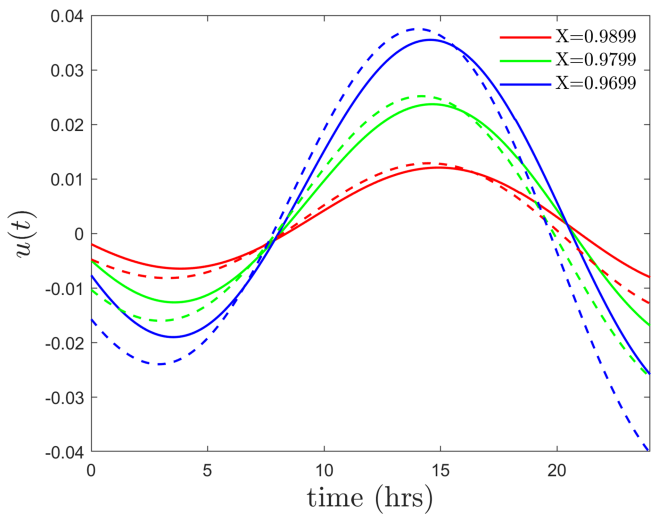

FIG. 8. Optimal inputs for various choices of X that minimize the cost functional (24) using a negative value for Δt are obtained using the reduced order equations inferred from the data-driven method. These optimal inputs are shown as solid lines. The dashed lines show nearly identical corresponding optimal inputs obtained using the exact values for the terms of the reduced order equations.

model describing the behavior of N coupled circadian oscillators,

$$\begin{aligned}\dot{a}_i &= h_1\frac{K_1^n}{K_1^n + c_i^n} - h_2\frac{a_i}{K_2 + a_i} + h_c\frac{KF(t)}{KF(t) + K_c}\\ &\quad + s_i(L_e(t + h(T_e)\Delta t) + u(t)) + \sqrt{2D}\eta_i(t),\\ \dot{b}_i &= h_3 a_i - h_4\frac{b_i}{K_4 + b_i},\\ \dot{c}_i &= h_5 b_i - h_6\frac{c_i}{K_6 + c_i},\\ \dot{d}_i &= h_7 a_i - h_8\frac{d_i}{K_8 + d_i}\end{aligned} \tag{52}$$

for $i = 1, \ldots, N$. A version of this model was originally proposed in Ref. 16. Here, variables a_i represent concentrations of an mRNA clock gene; b_i and c_i represent the concentrations of the associated protein and nuclear form of the protein, respectively; and d_i is a neurotransmitter that provides coupling between cells. It is assumed that spatial transmission of the neurotransmitter is fast relative to dynamics of each oscillator yielding a mean-field coupling $F(t) = (1/N)\sum_{k=1}^{N} d_k(t)$. $\eta_i(t)$ is an independent and identically distributed, zero-mean white noise process and D sets its intensity. $L_e(t)$ is a periodic light–dark cycle that nominally entrains the oscillation to the 24-h light–dark cycle taking the form

$$L_e(t) = 0.005\left[\frac{1}{1 + \exp(-4(\mathrm{mod}(t, 24) - 6))} - \frac{1}{1 + \exp(-4(\mathrm{mod}(t, 24) - 18))}\right]. \tag{53}$$

The term $h(T_e)$ is the unit step function that switches at time T_e and is used to model sudden time shifts in the light–dark cycle to mimic rapid travel across Δt time zones. The input $u(t)$ is an effective control input that represents the effect of an additional light source. Each oscillator from (52) is assumed to have an intrinsic sensitivity to light s_i, drawn from a distribution $s_i = \max(1 + 0.4N(0, 1), 0)$, where $N(0, 1)$ is a normal distribution with unit variance and zero mean. Nominal parameter values are taken to be $n = 5, h_1 = 0.868, h_2 = 0.634, h_3 = 0.7, h_4 = 0.35, h_5 = 0.7, h_6 = 0.35, h_7 = 0.35, h_8 = 1, K_1 = 1, K_2 = 1, K_4 = 1, K_6 = 1, K_8 = 1, h_c = 1, K_c = 1$, and $K = 0.5$. The nominal values of h_1, h_2, h_c, and n are chosen so that the oscillator has an unperturbed period near 24 h, and the remaining nominal parameters are identical to those listed in the caption of Fig. 1 from Ref. 16. To incorporate heterogeneity, for each oscillator, the parameters k_3, k_5, k_7, v_4, v_6, and v_8 are drawn from a normal distribution with the mean being the nominal parameter value and a standard deviation equal to 0.01. We take $N = 3000$ oscillators and use $D = 0.0001$ for the noise intensity. For the model (52), we assume that we have the ability to record the observable

$$\bar{a}(t) = \sum_{k=1}^{N} a_k(t). \tag{54}$$

Note here that the operational reduction strategy detailed in Ref. 60 is derived assuming that the system observable is a state variable. Even though $\bar{a}(t)$ is not a state variable, as illustrated in Appendix A, an operational phase and isostable coordinate system can still be implemented here. We also emphasize that it would still be possible to identify a reduced order model and subsequently implement the proposed control strategy using a different observable provided that it gives an adequate representation of the aggregate model behavior.

When both $L_e(t)$ and $u(t)$ are zero, the model (52) has a stable limit cycle with period 24.3 h—these oscillations readily entrain to the 24-h light–dark cycle from (53). Once again, we will illustrate our optimal isostable control strategy derived in Sec. IV in order to hasten recovery from time shifts in the light–dark cycle. Because of the high dimensionality of the model (52), it is not computationally feasible to identify phase and isostable response curves using the adjoint-based methods from Refs. 5 and 64. As such, the data-driven phase-amplitude model inference strategy described in Appendix B must be used to infer the necessary reduced order models.

The data-driven model inference strategy is implemented with respect to the unperturbed periodic orbit that emerges when both $L_e(t)$ and $u(t)$ are set to zero. The threshold corresponding to $\theta^* = 0$ is defined to be the moment that $\bar{a}(t)$ crosses 0.045 with a positive slope. Using a sampling rate of $\Delta t = 0.04$ h, 432 separate oscillations are measured over one period. These are shown as colored lines in panel (a) of Fig. 9. The average value, γ, is taken to be the periodic orbit, with corresponding values of $\bar{a} - \gamma$ shown in panel (b). POD is applied to this data. Taking $m = 2$ POD modes yields the ratio $\sum_{j=1}^{2}\zeta_j / \sum_{j=1}^{\alpha}\zeta_j = 0.995$. As such, one phase and one isostable coordinate are sufficient for the reduced order equations. Decay rates associated with the update matrix A_m as part of Eq. (B4) are found to be $\lambda_1 = 0.65$ and $\lambda_2 = 1$, which correspond to the decay of the isostable coordinates and the phase dynamics, respectively. Continuing the strategy detailed in Appendix B,

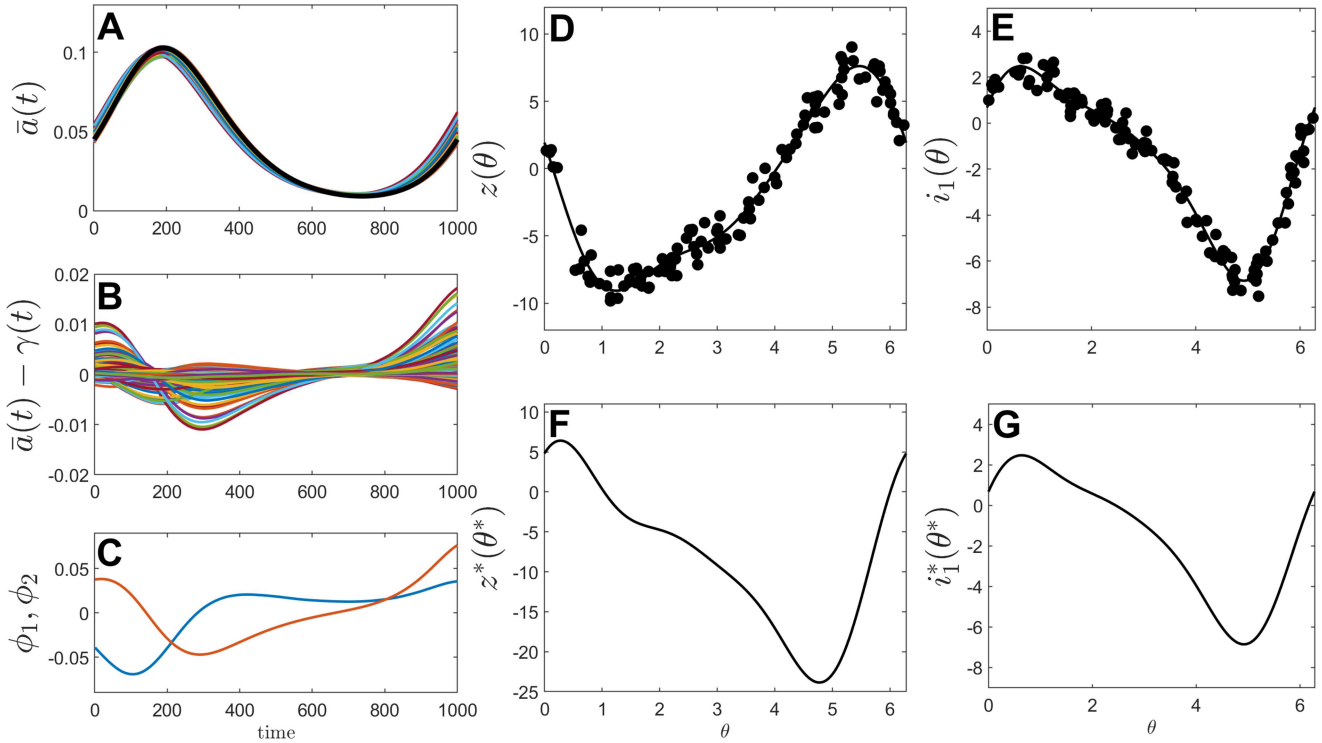

FIG. 9. Panel (a) shows 432 measurements of $\bar{a}(t)$ sampled over a single oscillation. The mean value is taken as the periodic orbit, γ, and shown as a black line. Panel (b) shows $\bar{a}(t) - \gamma(t)$ for each of these measurements. POD is performed on this dataset; in this application, the two modes shown in panel (c) are sufficient to capture this data. Panels (d) and (e) show results from the application of the direct model inference strategy described in Step 6 of Appendix B. Black dots show individual measurements, and the black lines are fit to the data. Panels (f) and (g) show the operational phase and isostable response curves calculated according to Eq. (13).

direct estimates of the phase and isostable response curves are obtained by applying finite perturbations of magnitude $u(t) = 0.01$ lasting for 3 h. The subsequent shift in the isostable and phase coordinates is computed according to Eqs. (B5) and (B6), respectively, with individual trials represented as black dots in panels (d) and (e) of Fig. 9. Phase and isostable response curves (black lines) are obtained by fitting these data to a sinusoidal basis of the form $\sum_{n=0}^{3}[a_n \sin(n\theta) + b_n \cos(n\theta)]$. The associated terms of the operational phase and isostable reduction are shown in panels (f) and (g), with curves calculated according to Eq. (13). The value $\alpha_1 = -0.0763$ associated with the operational phase and isostable reduction (12) is inferred by finding a least-squares fit to the relationship (B8).

After inferring the operational phase and isostable reduced order model for (52), we turn our attention to the problem of identifying an energy optimal stimulus that can be used to hasten recovery from circadian misalignment following a time shift in the external stimulus. Recalling from Eq. (25) that shifting the isostable coordinates by $\Delta\psi$ will yield a latent phase shift $-\frac{\alpha_1 \Delta\psi_1}{\kappa_1}$, and given that $\alpha_1 < 0$, recovery from a negative (respectively, positive) time shift in the entraining stimulus is expected to be hastened by shifting to more positive (respectively, negative) isostable coordinates. Minimizing the cost functional from (24) balances the trade-off between maximizing the latent phase shift (to hasten recovery) and minimizing the L^2 norm of the applied input. The calculus of variations approach from Sec. IV B is applied using $T_e = 24$ h. Resulting optimal inputs are shown in panels (a) and (b) of Fig. 10 for negative and positive values of Δt, respectively. As in the previous example, each input is designed to be applied starting at $\mathrm{mod}(t, 24) = 0$ from an initial condition located on the fully entrained orbit. After applying these optimal inputs to the full model, the resulting values of $\psi_1(24)$ and $\theta^*(24)$ are inferred according to the relations (B5) and (B6). These values are subtracted from the nominal values on the entrained periodic orbit, with results shown in panel (c) of Fig. 10. This control input is able to yield isostable coordinate shifts of between -0.14 and 0.06 with only minor changes in the operational phase coordinate. As the amplitude of the inputs becomes larger, unmodeled nonlinearities in the full model equations begin to degrade the performance.

Finally, for the full model equations (52), reentrainment following the application of the optimal stimuli is investigated. To measure the recovery times, the full model equations (52) are simulated with $u(t) = 0$ until the oscillation is fully entrained to the 24-h light–dark cycle. For a given choice of X, the corresponding optimal stimulus is applied over a 24-h period resulting in an associated shift in isostable coordinate $\Delta\psi_1$. After this initial 24-h period, time is shifted by

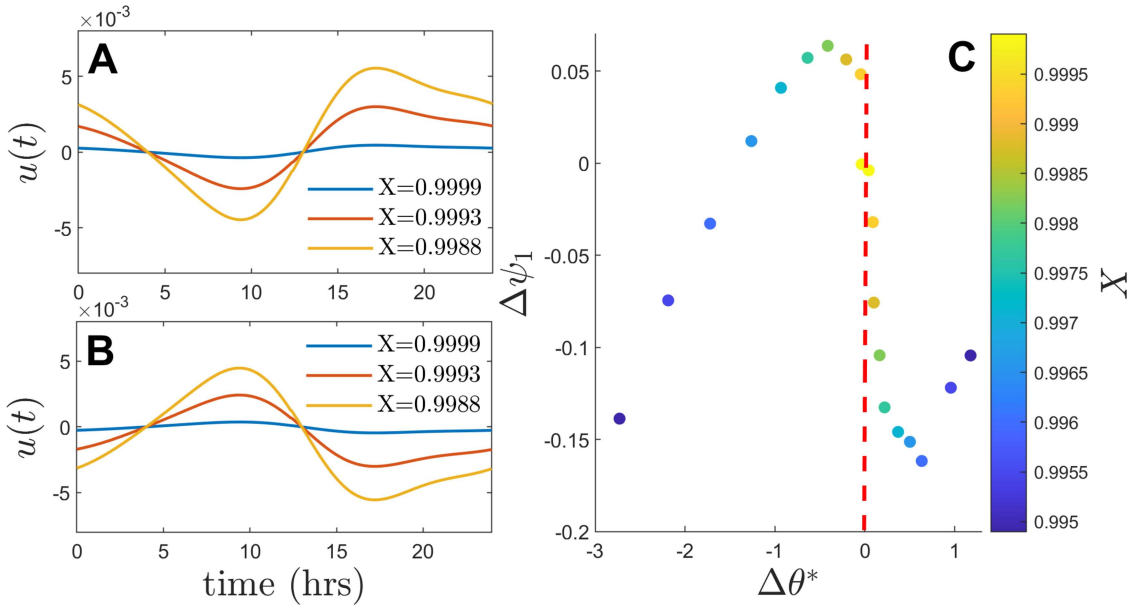

FIG. 10. Panels (a) [respectively, (b)] show optimal control inputs that minimize the cost functional (24) for negative (respectively, positive) time shifts using various values of the weighting parameter X. Note here that the sign of Δt sets the form of the cost functional from Eq. (24), which ultimately determines the sign of the target isostable coordinate. In simulations of the full model (52), these inputs are applied starting from a fully entrained initial condition, and the resulting change in the operational phase and isostable coordinate is shown in panel (c). For smaller magnitude inputs (associated with values of X close to 1), the resulting inputs yield the desired shifts in the isostable coordinates without modifying θ^*. For larger magnitude inputs, unmodeled nonlinearities result in undesired shifts in θ^*. In panel (c), the resulting optimal stimuli are being evaluated with respect to their ability to satisfy the constraints of the optimal control problem, i.e., to shift the isostable coordinate without yielding a net change in the operational phase. Resulting recovery times for specific time shifts are illustrated in Fig. 11.

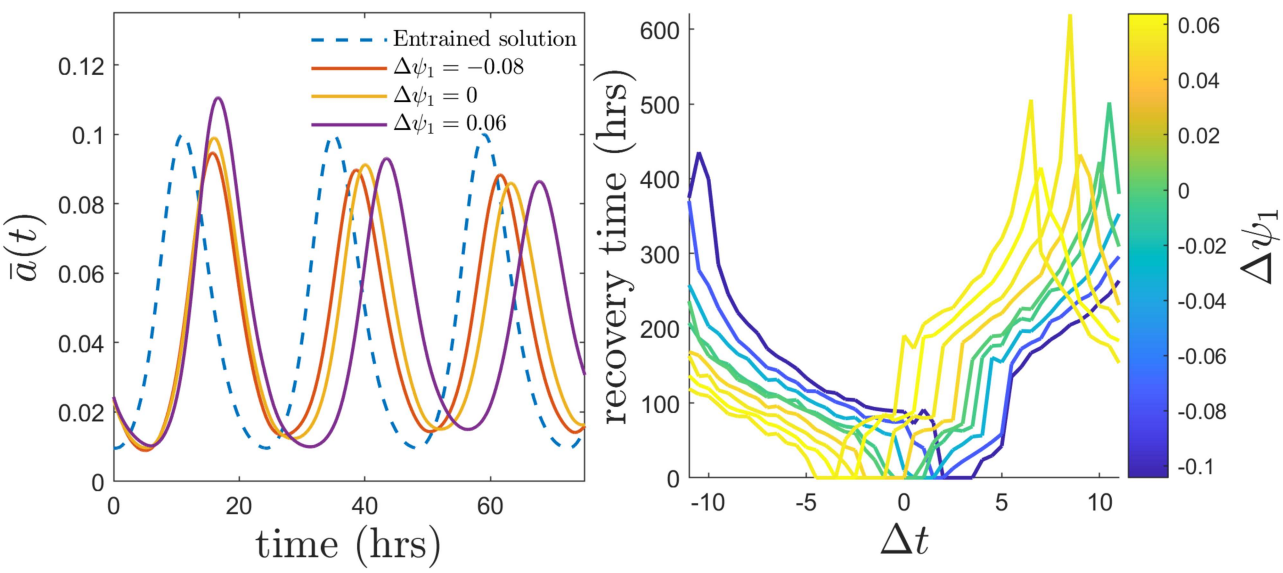

FIG. 11. The left panel illustrates reentrainment after a time shift $\Delta t = +5$ h occurring at $T_e = 24$ following the application of three different inputs on $t \in [0, 24]$ that yield different values of $\Delta\psi_1$. For reference, the dashed blue line shows a solution that is fully entrained in the shifted time zone. As shown in the right panel, optimal inputs that shift the isostable coordinates to more positive (respectively, negative) values reduce the recovery times resulting from negative (respectively, positive) shifts in the external time. Note that these optimal inputs do not significantly change θ^*.

Δt to mimic rapid travel through multiple time zones. The time required to recover to within 1 h of the fully entrained solution is recorded, with results shown in the right panel of Fig. 11. These results are qualitatively similar to those from Fig. 6 for the nonradial isochron clock. Once again, the recovery time curve is shifted in proportion to the resulting isostable coordinate shift. As predicted, positive (respectively, negative) isostable coordinate shifts result in hastened recovery from negative (respectively, positive) Δt shifts. The left panel shows traces of $\bar{a}(t)$ in response to a $\Delta t = +5$ h time shift after the indicated optimal stimulus is applied.

VI. CONCLUSION

In this work, we investigate the influence of circadian memory in the context of recovery from circadian misalignment. We use an operational phase and isostable reduced order modeling framework to capture the behavior of slowly decaying amplitude coordinates that depend on the past input history. By analyzing the operational phase and isostable reduced equations, we identify a latent phase shift highlighted in (25) that is directly proportional to the isostable coordinates and can be used to prime the underlying system to recover more rapidly to an expected shift in the environmental time. A subsequent optimal control formulation is proposed that balances the trade-off between control effort and the resulting latent phase shift. Explicit, approximate solutions for this optimal control problem are also derived that are valid in the limit that the magnitude of the input is small. The resulting control strategy is validated on a simple model (51) that exhibits entrained oscillations and a more complicated model (52) that considers the aggregate behavior of entrained coupled oscillators. In both of these models, the operational phase-amplitude reduced equations are successfully inferred using data-driven techniques that would be necessary in experimental settings where the full model equations are unknown.

The proposed control strategy to hasten recovery from circadian misalignment differs from previously considered control frameworks in its explicit consideration of memory effects. In contrast, many previously considered control strategies (e.g., Refs. 3, 13, 47, and 67) seek to find inputs that will hasten realignment in response to a time shift when starting from a nominally fully entrained state. Other pretreatment strategies[7,12,44] have been proposed to shift the nominal phase prior to expected travel across multiple time zones but do not consider amplitude-based effects. The proposed strategy is designed to modify the amplitude coordinates associated with a nominally entrained oscillation *without changing the phase prior to the expected time shift*; here, the associated latent phase shift influences the subsequent recovery. In this work, in order to isolate the influence of the isostable coordinates on the recovery from circadian misalignment, optimal solutions of the cost functional (24) are required to satisfy $\Delta\theta^*(T_e) = 0$; that is, optimal inputs are not allowed to modify θ^*. It would be of interest in future work to consider solutions for which $\Delta\theta^*(T_e)$ could take nonzero values. This would certainly allow for faster recovery from circadian misalignment by both shifting the operational phase and the latent phase appropriately.

There are many limitations that this paper does not directly consider. Foremost, while the model used to represent coupled circadian oscillations from (52) is high-dimensional and complex from a dynamical systems perspective, it does not accurately capture the complicated physiologically relevant processes governing circadian rhythms. More detailed models of gene regulation such as Refs. 24, 28, 33, and 41 would be necessary to investigate the influence of circadian memory on recovery from circadian misalignment. Additionally, the operational phase and isostable reduced order models used in this work are only valid to first order accuracy in the amplitude coordinates. As such, the resulting optimal control inputs are required to be sufficiently small so that the validity of the reduced order model is not degraded. It would be of interest to extend this control framework for phase-isostable-based models that are valid to higher orders of accuracy such as those from Ref. 58 or Ref. 56. Also, practical implementation of the data-driven model inference strategies suggested in this work would require thousands of separate 24-h measurements of circadian cycles to infer the associated operational phase and isostable reduced order models. This would be prohibitive in an experimental setting unless recordings could be taken in parallel from different subjects. To alleviate this issue, it would be of interest to develop more efficient data-driven model inference techniques that require less data. These and other practical considerations will be investigated in future work.

ACKNOWLEDGMENTS

This material is based upon work supported by the National Science Foundation (NSF) under Grant No. CMMI-1933583.

APPENDIX A: OPERATIONAL PHASE COORDINATES FOR ARBITRARY OBSERVABLES

In Ref. 60, the idea of an operational phase coordinate, θ^*, was introduced by defining $\theta^* = 0$ to correspond to the level set of a system state. In many cases, including the example from Sec. V C, no system states are directly measurable. Here, we illustrate that operational coordinates can still be defined in reference to a general system observable. Additionally, we show that similar relationships between standard phase response curves and operational phase response curves still hold when a general system observable is used.

Following a derivation similar to Ref. 60, consider a T-periodic, stable limit cycle, γ, of a general dynamical system of the form

$$\dot{x} = F(x, p_0) + U(t), \tag{A1}$$

where $x \in \mathbb{R}^N$ is the state, $p_0 \in \mathbb{R}$ is a nominal parameter, F gives the dynamics, and $U(t)$ is an additive input. When taking $U(t) = 0$, let θ denote the asymptotic phase for the model (A1) defined according to the isochrons from (3) and let $x^\gamma(0)$ be defined as the intersection γ and the $\theta = 0$ isochron. We will take $y(x) \in \mathbb{R}$ to be a system observable and define the $\theta^*(x) = 0$ level set to be all states x in the neighborhood of $x^\gamma(0)$ for which $y(x) = y(x^\gamma(0))$ and $\text{sign}\left(\frac{dy}{dt}|_x\right) = \text{sign}\left(\frac{dy}{dt}|_{x^\gamma(0)}\right)$. Continuing to mirror the derivation from Ref. 60, we suppose that a dynamical relationship between an operational phase and the isostable coordinates exists that follows

$$\dot{\theta}^* = \omega + d(\psi_1, \ldots, \psi_{N-1}) + \left.\frac{\partial \theta^*}{\partial x}^T\right|_{x(t)} U(t), \tag{A2}$$

where $\omega = 2\pi/T, \theta^*(x) \in [0, 2\pi)$, and d is a function of the isostable coordinates. As discussed in Ref. 60, it is straightforward to show by contradiction that $d(0, \ldots, 0) = 0$. Consequently, $\theta^*(x) = \theta(x)$ for all $x \in \gamma$.

For the moment, we will take $U = 0$. Noting that $\dot{\theta} = \omega$ when $U = 0$, taking the integral of $\frac{d}{dt}(\theta^*(t) - \theta(t))$ in the limit that time approaches infinity yields

$$\theta^*(0) = \theta(0) - \int_0^\infty d(\psi_1, \ldots, \psi_{N-1})dt. \tag{A3}$$

Expanding $d(\psi_1, \ldots, \psi_N)$ on a basis of isostable coordinates, provided each isostable is an $O(\epsilon)$ term where $0 < \epsilon \ll 1$, to leading order, one can write

$$d(\psi_1, \ldots, \psi_N) = \sum_{j=1}^{N-1} \alpha_j \psi_j + O(\epsilon^2), \tag{A4}$$

where each α_j is a term in the Taylor expansion. With this setup, one can mirror the derivation from Sec. II of Ref. 60 to yield the operational phase and the isostable reduced order set of equations identical to those from (11).

As a final note, the main equation considered in (1) uses parameter perturbations and not additive perturbations as in (A1). Nevertheless, as done in Eq. (6), taking $p(t) - p_0$ to be an order ϵ term, one can rewrite (1) as

$$\dot{x} = F(x, p_0) + U(t) + O(\epsilon^2) \tag{A5}$$

to yield the required form where $U(t) = \frac{\partial F}{\partial p}(p(t) - p_0)$ with partial derivatives evaluated at x and p_0.

APPENDIX B: DATA-DRIVEN INFERENCE PHASE AND ISOSTABLE DYNAMICS

Adjoint-based methods for computing phase and isostable response curves as discussed in Refs. 5 and 64 can be implemented straightforwardly when dynamical equations of the underlying model (1) are known. By contrast, when the dynamical equations are unknown, the necessary terms of the phase reduction must be inferred using data-driven techniques. For example, for a standard phase reduction with equations of the form (9), a so-called "direct method" can be implemented to infer $Z(\theta)$ by measuring the phase change in response to a set of impulse perturbations applied at many different phases.[14,21,36] The authors of Ref. 61 proposed a related strategy to infer the terms of associated isostable reduced equations from (10); however, this strategy can only be implemented when a single isotable coordinate is sufficient to characterize the transient behavior. More recently, a strategy was proposed in Ref. 57 that can be used to infer phase-isostable reduced equations in situations where multiple isostable coordinates may be required. This framework is applied in the applications considered in Sec. V of this work with details summarized below.

To begin, consider a general dynamical system of the form

$$\begin{aligned} \dot{x} &= F(x, p(t)) + \epsilon\eta(t), \\ y(t) &= G(x), \end{aligned} \tag{B1}$$

where $x \in \mathbb{R}^N$ is the state, $y \in \mathbb{R}$ is a single system observable, $\eta(t) = [\eta_1(t), \ldots, \eta_N(t)]^T$ with each component $\eta_i(t)$ being an independent Gaussian white noise process with intensity D_i, F gives the nominal dynamics, $p \in \mathbb{R}$ is a parameter, G maps the state to an observable, and $0 < \epsilon \ll 1$. Correlations between the noise processes, colored noise processes, and influences of measurement noise are not considered in (B1). Suppose that in the absence of noise, when taking a constant $p(t) = p_0$, (B1) admits a stable T-periodic orbit. Here, the dynamics governing Eq. (B1) are identical to those of (1) except for the explicit addition of small magnitude, additive Gaussian noise applied independently to each state variable. A phase-isostable-based reduced order model can be inferred in a data-driven manner using the following procedure, adapted from Ref. 57:

Step 1. Choose some threshold that defines the Poincaré section that defines the $\theta^* = 0$ level set. Drawing on the relation from Eq. (15), $\theta \approx 0$ when $\theta^* = 0$ provided that the isostable coordinates remain small. After allowing any transient behavior to die out, T can be estimated by taking the average time between crossings of the $\theta^* = 0$ threshold.

Step 2. Consider a collection of υ sets of data signals $y_1, y_2, \ldots, y_\upsilon \in \mathbb{R}^\xi$ arranged as column vectors and taken in the interval $[t_i, t_i + T]$ so that their first components correspond to an initial condition $y_i(t_i)$ for which θ^* is close to 0 and the remaining $\xi - 1$ measurements are taken $\Delta t = \frac{T}{\xi - 1}$ time units apart. In other words, each y_i represents a recording over one period with $\theta^*(t_i) \approx 0$. Note that using an initial condition for which $\theta^*(t_i) \approx 0$ and not $\theta^*(t_i) = 0$ allows for better inference of the Floquet eigenmode associated with the unity Floquet multiplier. Take $\gamma = \frac{1}{\upsilon}\sum_{i=1}^{\upsilon} y_i$ to be the nominal periodic orbit and define the matrix $B \in \mathbb{R}^{\xi,\upsilon}$ to be

$$B \equiv [y_1 - \gamma, \ldots, y_\upsilon - \gamma]. \tag{B2}$$

Also, let $b_j = y_j - \gamma$.

Step 3. Proper orthogonal decomposition (POD)[20] is employed, which is a well-established framework used to decompose a set of data snapshots into a smaller number of representative modes. Individual POD modes, ϕ_j, can be found using the method of snapshots according to[20]

$$\phi_j = \frac{1}{\sqrt{\zeta_j}} B v_j, \tag{B3}$$

where v_j and ζ_j denote the eigenvectors and eigenvalues, respectively, of the matrix $B^T B$, with eigenvalues ordered such that $\zeta_j > \zeta_{j+1}$. The resulting basis of POD modes is orthogonal and is arranged so that modes associated with larger values of ζ_j capture more of the temporal fluctuations in the data set. A reduced set of m modes are chosen such that $\sum_{j=1}^{m} \zeta_j / \sum_{j=1}^{\alpha} \zeta_j \approx 1$. One can define $\Phi \in \mathbb{R}^{\xi \times m}$ such that $\Phi = [\phi_1 \ \ldots \ \phi_m]$. Likewise, let $M_i = \Phi^T b_i$ be a vector of POD coefficients associated with the embedding b_i.

Step 4. In order to infer phase and isostable dynamics, it is necessary to understand how the POD modes change over time. To this end, for each y_i from Step 2, one can consider a set of complementary measurements y_i^+, taken over the time

interval $[t_i + T, t_i + 2T]$. Let $M_i^+ = \Phi^T(y_i^+ - \gamma)$ be the associated POD coefficients. We seek to infer the matrix A_M that captures the general relationship

$$M_i^+ = A_M M_i. \tag{B4}$$

Letting $B^+ \in \mathbb{R}^{\xi,\upsilon} \equiv [y_1^+ - \gamma, \ldots, y_\upsilon^+ - \gamma]$, the matrix A_M can be estimated using the relationship $A_M = (\Phi^T B^+)(\Phi^T B)^\dagger$.

Step 5. Letting λ_i^{DD}, w_i^{DD}, and v_i^{DD} denote the eigenvalues, left eigenvectors, and right eigenvectors of A_M, respectively, consider any signal $y = [y(t_L)\ y(t_L + \Delta t)\ \ldots]^T$ with samples taken at intervals $\Delta t = T/(\beta - 1)$ that begin at $t = t_L$. Letting t_k correspond to a time that the signal y crosses the $\theta^* = 0$ level set, and letting $s_k \in \mathbb{R}^\xi = [y(t_k)y(t_k + \Delta T), \ldots, y(t_k + T)]^T$, an isostable coordinate $\psi_j(t_L)$ can be inferred for any $\lambda_j^{DD} \neq 1$ according to the relationship

$$\psi_j(t_L) = (w_j^{DD})^T \Phi^T(s_k - \gamma) \exp\left(-\frac{\log(\lambda_j^{DD})(t_k - t_L)}{T}\right). \tag{B5}$$

Additionally, there will be one eigenvalue $\lambda_m^{DD} = 1$ that characterizes the phase dynamics. The corresponding phase coordinate can be found according to

$$\theta(t_L) = 2\pi\left(1 - \frac{t_k - t_L}{T}\right) + \frac{1}{c}(w_m^{DD})^T \Phi^T(s_k - \gamma), \tag{B6}$$

where, as discussed in Ref. 57, c is a constant that is chosen so that $\dot{\theta} = 2\pi/T$ in the absence of noise and input.

Step 6. Taking $\omega = 2\pi/T$ and each $\kappa_j = \log(\lambda_j^{DD})/T$, the functions of the phase-isostable reduction (9) and (10) can be inferred using a strategy similar to the direct method.[14,21,36] Specifically, by first taking $u(t) = 0$ and allowing transient behavior to die out so that each ψ_j is zero (corresponding to the state being on the periodic orbit), a perturbation $u(t) = u_M$ can be applied on the interval $t_0 \leq t \leq t_L$ at some known $\theta_0(t_0)$. The resulting change to each of the isostable and phase coordinate ($\Delta\psi_j$ and $\Delta\theta$, respectively) can then be measured from the response using the relations given in (B5) and (B6), respectively. An approximation for a single data point on each isostable and phase response curve can then be obtained according to $i_j(\theta_0) = \frac{\Delta\psi_j}{u_M(t_L - t_0)}$ and $z(\theta_0) = \frac{\Delta\theta}{u_M(t_L - t_0)}$, respectively. This process can be repeated over multiple measurements by applying perturbations at different initial phases, and the resulting data points can be fit to an appropriate periodic basis.

The above procedure allows for the inference of phase-isostable-based reduced order models of the form (9) and (10). In this work, we are also interested in using operational phase and isostable reduced models of the form (12), which require estimation of each α_j. Such estimates can be obtained, for instance, as part of Step 6 in the above procedure by recalling that m is the number of modes required in Step 3 and noticing that

$$\dot{\theta}^* - \dot{\theta} = \sum_{j=1}^{m-1} \alpha_j \psi_j \tag{B7}$$

results from subtracting the operational phase equations in (12) from (9). Immediately after each perturbation from Step 6, the dynamics of each isostable coordinate follow $\psi_j(t) = \psi_j(t_L)\exp(\kappa_j(t - t_L))$. Using this information and recalling that $\theta^* = \theta$ when the state is on the limit cycle, directly integrating (B7) yields

$$\theta^*(t) - \theta(t) = \sum_{j=1}^{m-1}\left(\frac{\alpha_j \psi_j(t_L)}{\kappa_j}\exp(\kappa_j(t - t_L))\right). \tag{B8}$$

Direct measurements of θ^* can be taken at every crossing of the $\theta^* = 0$ level set. Estimates of $\theta(t)$ can be taken by noting that $\theta^* - \theta$ approaches 0 as the trajectory decays to the periodic orbit and using the fact that $\theta(t) = \theta(t_L) + \omega(t - t_L)$ in the absence of input. Each $\psi_j(t_L)$ can be estimated according to (B5), leaving the α_j terms as the only unknowns in (B8), which can be fit to the data.

DATA AVAILABILITY

The data that support the findings of this study are available from the corresponding author upon reasonable request.

REFERENCES

[1] S. An, R. Harang, K. Meeker, D. Granados-Fuentes, C. A. Tsai, C. Mazuski, J. Kim, F. J. Doyle, L. R. Petzold, and E. D. Herzog, "A neuropeptide speeds circadian entrainment by reducing intercellular synchrony," Proc. Natl. Acad. Sci. U.S.A. **110**(46), E4355–E4361 (2013).

[2] J. Arendt, "Managing jet lag: Some of the problems and possible new solutions," Sleep Med. Rev. **13**(4), 249–256 (2009).

[3] N. Bagheri, J. Stelling, and F. J. Doyle III, "Circadian phase resetting via single and multiple control targets," PLoS Comput. Biol. **4**(7), e1000104 (2008).

[4] M. Beaumont, D. Batejat, C. Pierard, P. Van Beers, J. B. Denis, O. Coste, P. Doireau, F. Chauffard, J. French, and D. Lagarde, "Caffeine or melatonin effects on sleep and sleepiness after rapid eastward transmeridian travel," J. Appl. Physiol. **96**(1), 50–58 (2004).

[5] E. Brown, J. Moehlis, and P. Holmes, "On the phase reduction and response dynamics of neural oscillator populations," Neural Comput. **16**(4), 673–715 (2004).

[6] S. A. Brown, F. Fleury-Olela, E. Nagoshi, C. Hauser, C. Juge, C. A. Meier, R. Chicheportiche, J. M. Dayer, U. Albrecht, and U. Schibler, "The period length of fibroblast circadian gene expression varies widely among human individuals," PLoS Biol. **3**(10), e338 (2005).

[7] H. J. Burgess, S. J. Crowley, C. J. Gazda, L. F. Fogg, and C. I. Eastman, "Preflight adjustment to eastward travel: 3 days of advancing sleep with and without morning bright light," J. Biol. Rhythms **18**(4), 318–328 (2003).

[8] H. J. Burgess, V. L. Revell, and C. I. Eastman, "A three pulse phase response curve to three milligrams of melatonin in humans," J. Physiol. **586**(2), 639–647 (2008).

[9] A. L. Chesson, M. Littner, D. Davila, W. M. Anderson, M. Grigg-Damberger, K. Hartse, S. Johnson, and M. Wise, "Practice parameters for the use of light therapy in the treatment of sleep disorders," Sleep **22**(5), 641–660 (1999).

[10] C. A. Czeisler, J. F. Duffy, T. L. Shanahan, E. N. Brown, J. F. Mitchell, D. W. Rimmer, J. M. Ronda, E. J. Silva, J. S. Allan, J. S. Emens, D. J. Dijk, and R. E. Kronauer, "Stability, precision, and near-24-hour period of the human circadian pacemaker," Science **284**(5423), 2177–2181 (1999).

[11] J. A. Daymude and R. Refinetti, "Phase-shifting effects of single and multiple light pulses in the golden hamster," Biol. Rhythm Res. **30**(2), 202–215 (1999).

[12] S. Deacon and J. Arendt, "Adapting to phase shifts, I. An experimental model for jet lag and shift work," Physiol. Behav. **59**(4–5), 665–673 (1996).

[13] D. A. Dean, D. B. Forger, and E. B. Klerman, "Taking the lag out of jet lag through model-based schedule design," PLoS Comput. Biol. **5**(6), e1000418 (2009).

[14] R. F. Galán, G. B. Ermentrout, and N. N. Urban, "Efficient estimation of phase-resetting curves in real neurons and its significance for neural-network modeling," Phys. Rev. Lett. **94**(15), 158101 (2005).

[15]D. A. Golombek and R. E. Rosenstein, "Physiology of circadian entrainment," Physiol. Rev. **90**(3), 1063–1102 (2010).
[16]D. Gonze, S. Bernard, C. Waltermann, A. Kramer, and H. Herzel, "Spontaneous synchronization of coupled circadian oscillators," Biophys. J. **89**(1), 120–129 (2005).
[17]J. Guckenheimer, "Isochrons and phaseless sets," J. Math. Biol. **1**(3), 259–273 (1975).
[18]T. Harada, H. A. Tanaka, M. J. Hankins, and I. Z. Kiss, "Optimal waveform for the entrainment of a weakly forced oscillator," Phys. Rev. Lett. **105**(8), 088301 (2010).
[19]M. Hébert, S. K. Martin, C. Lee, and C. I. Eastman, "The effects of prior light history on the suppression of melatonin by light in humans," J. Pineal Res. **33**(4), 198–203 (2002).
[20]P. Holmes, J. L. Lumley, G. Berkooz, and C. W. Rowley, *Turbulence, Coherent Structures, Dynamical Systems and Symmetry* (Cambridge University Press, 2012).
[21]E. M. Izhikevich, *Dynamical Systems in Neuroscience: The Geometry of Excitability and Bursting* (MIT Press, London, 2007).
[22]D. Jordan and P. Smith, *Nonlinear Ordinary Differential Equations: An Introduction for Scientists and Engineers* (Oxford University Press, Oxford, 2007), Vol. 10.
[23]S. B. S. Khalsa, M. E. Jewett, C. Cajochen, and C. A. Czeisler, "A phase response curve to single bright light pulses in human subjects," J. Physiol. **549**(3), 945–952 (2003).
[24]J. K. Kim and D. B. Forger, "A mechanism for robust circadian timekeeping via stoichiometric balance," Mol. Syst. Biol. **8**(1), 630 (2012).
[25]D. Kirk, *Optimal Control Theory* (Dover Publications, New York, 1998).
[26]Y. Kuramoto, *Chemical Oscillations, Waves, and Turbulence* (Springer-Verlag, Berlin, 1984).
[27]M. D. Kvalheim and S. Revzen, "Existence and uniqueness of global Koopman eigenfunctions for stable fixed points and periodic orbits," arXiv preprint 1911.11996, 2019.
[28]J. C. Leloup and A. Goldbeter, "Toward a detailed computational model for the mammalian circadian clock," Proc. Natl. Acad. Sci. U.S.A. **100**(12), 7051–7056 (2003).
[29]J. C. Leloup and A. Goldbeter, "Critical phase shifts slow down circadian clock recovery: Implications for jet lag," J. Theor. Biol. **333**, 47–57 (2013).
[30]A. J. Lewy, V. K. Bauer, S. Ahmed, K. H. Thomas, N. L. Cutler, C. M. Singer, M. T. Moffit, and R. L. Sack, "The human phase response curve (PRC) to melatonin is about 12 hours out of phase with the PRC to light," Chronobiol. Int. **15**(1), 71–83 (1998).
[31]I. Mezić, "Spectrum of the Koopman operator, spectral expansions in functional spaces, and state-space geometry," J. Nonlinear Sci. **30**, 2091–2145 (2020).
[32]D. S. Minors, J. M. Waterhouse, and A. Wirz-Justice, "A human phase-response curve to light," Neurosci. Lett. **133**(1), 36–40 (1991).
[33]H. P. Mirsky, A. C. Liu, D. K. Welsh, S. A. Kay, and F. J. Doyle, "A model of the cell-autonomous mammalian circadian clock," Proc. Natl. Acad. Sci. U.S.A. **106**(27), 11107–11112 (2009).
[34]B. Monga, D. Wilson, T. Matchen, and J. Moehlis, "Phase reduction and phase-based optimal control for biological systems: A tutorial," Biol. Cybern. **113**(1–2), 11–46 (2019).
[35]R. Y. Moore, J. C. Speh, and R. K. Leak, "Suprachiasmatic nucleus organization," Cell Tissue Res. **309**(1), 89–98 (2002).
[36]T. Netoff, M. A. Schwemmer, and T. J. Lewis, "Experimentally estimating phase response curves of neurons: Theoretical and practical issues," in *Phase Response Curves in Neuroscience* (Springer, 2012), pp. 95–129.
[37]University of Michigan, see http://entrain.math.lsa.umich.edu for "Entrain Yourself"; accessed 15 July 2019.
[38]C. Piérard, M. Beaumont, M. Enslen, F. Chauffard, D. X. Tan, R. J. Reiter, A. Fontan, J. French, O. Coste, and D. Lagarde, "Resynchronization of hormonal rhythms after an eastbound flight in humans: Effects of slow-release caffeine and melatonin," Eur. J. Appl. Physiol. **85**(1–2), 144–150 (2001).
[39]K. Pyragas, A. P. Fedaravičius, T. Pyragienė, and P. A. Tass, "Optimal waveform for entrainment of a spiking neuron with minimum stimulating charge," Phys. Rev. E **98**(4), 042216 (2018).
[40]R. Refinetti, "Compression and expansion of circadian rhythm in mice under long and short photoperiods," Integr. Physiol. Behav. Sci. **37**(2), 114–127 (2002).
[41]A. Relógio, P. O. Westermark, T. Wallach, K. Schellenberg, A. Kramer, and H. Herzel, "Tuning the mammalian circadian clock: Robust synergy of two loops," PLoS Comput. Biol. **7**(12), e1002309 (2011).
[42]S. M. Reppert and D. R. Weaver, "Coordination of circadian timing in mammals," Nature **418**(6901), 935 (2002).
[43]V. L. Revell, H. J. Burgess, C. J. Gazda, M. R. Smith, L. F. Fogg, and C. I. Eastman, "Advancing human circadian rhythms with afternoon melatonin and morning intermittent bright light," J. Clin. Endocrinol. Metab. **91**(1), 54–59 (2006).
[44]V. L. Revell and C. I. Eastman, "How to trick mother nature into letting you fly around or stay up all night," J. Biol. Rhythms **20**(4), 353–365 (2005).
[45]R. L. Sack, "Jet lag," N. Engl. J. Med. **362**(5), 440–447 (2010).
[46]C. H. Samuels, "Jet lag and travel fatigue: A comprehensive management plan for sport medicine physicians and high-performance support teams," Clin. J. Sport Med. **22**(3), 268–273 (2012).
[47]K. Serkh and D. B. Forger, "Optimal schedules of light exposure for rapidly correcting circadian misalignment," PLoS Comput. Biol. **10**(4), e1003523 (2014).
[48]K. Shimomura and M. Menaker, "Light-induced phase shifts in tau mutant hamsters," J. Biol. Rhythms **9**(2), 97–110 (1994).
[49]S. Shirasaka, W. Kurebayashi, and H. Nakao, "Phase-amplitude reduction of transient dynamics far from attractors for limit-cycling systems," Chaos **27**(2), 023119 (2017).
[50]A. Suhner, P. Schlagenhauf, R. Johnson, A. Tschopp, and R. Steffen, "Comparative study to determine the optimal melatonin dosage form for the alleviation of jet lag," Chronobiol. Int. **15**(6), 655–666 (1998).
[51]S. R. Taylor, R. Gunawan, L. R. Petzold, and F. J. Doyle III, "Sensitivity measures for oscillating systems: Application to mammalian circadian gene network," IEEE Trans. Automat. Contr. **53**, 177–188 (2008).
[52]H. T. vanderLeest, J. H. T. Rohling, S. Michel, and J. H. Meijer, "Phase shifting capacity of the circadian pacemaker determined by the SCN neuronal network organization," PLoS One **4**(3), e4976 (2009).
[53]J. Waterhouse, T. Reilly, G. Atkinson, and B. Edwards, "Jet lag: Trends and coping strategies," Lancet **369**(9567), 1117–1129 (2007).
[54]S. Wiggins, *Introduction to Applied Nonlinear Dynamical Systems and Chaos* (Springer, 2003), Vol. 2.
[55]D. Wilson, "Isostable reduction of oscillators with piecewise smooth dynamics and complex Floquet multipliers," Phys. Rev. E **99**(2), 022210 (2019).
[56]D. Wilson, "An adaptive phase-amplitude reduction framework without $\mathcal{O}(\epsilon)$ constraints on inputs," arXiv:2011.10410 (2020).
[57]D. Wilson, "A data-driven phase and isostable reduced modeling framework for oscillatory dynamical systems," Chaos **30**(1), 013121 (2020).
[58]D. Wilson, "Phase-amplitude reduction far beyond the weakly perturbed paradigm," Phys. Rev. E **101**(2), 022220 (2020).
[59]D. Wilson and B. Ermentrout, "Greater accuracy and broadened applicability of phase reduction using isostable coordinates," J. Math. Biol. **76**(1–2), 37–66 (2018).
[60]D. Wilson and B. Ermentrout, "An operational definition of phase characterizes the transient response of perturbed limit cycle oscillators," SIAM J. Appl. Dyn. Syst. **17**(4), 2516–2543 (2018).
[61]D. Wilson and B. Ermentrout, "Augmented phase reduction of (not so) weakly perturbed coupled oscillators," SIAM Rev. **61**(2), 277–315 (2019).
[62]D. Wilson, A. B. Holt, T. I. Netoff, and J. Moehlis, "Optimal entrainment of heterogeneous noisy neurons," Front. Neurosci. **9**, 192 (2015).
[63]D. Wilson and J. Moehlis, "An energy-optimal approach for entrainment of uncertain circadian oscillators," Biophys. J. **107**(7), 1744–1755 (2014).
[64]D. Wilson and J. Moehlis, "Isostable reduction of periodic orbits," Phys. Rev. E **94**(5), 052213 (2016).
[65]A. Winfree, *The Geometry of Biological Time*, 2nd ed. (Springer-Verlag, New York, 2001).
[66]K. P. Wright, R. J. Hughes, R. E. Kronauer, D. J. Dijk, and C. A. Czeisler, "Intrinsic near-24-h pacemaker period determines limits of circadian entrainment to a weak synchronizer in humans," Proc. Natl. Acad. Sci. U.S.A. **98**(24), 14027–14032 (2001).
[67]J. Zhang, A. Bierman, J. T. Wen, A. Julius, and M. Figueiro, "Circadian system modeling and phase control," in *2010 49th IEEE Conference on Decision and Control* (IEEE, 2010), pp. 6058–6063.
[68]A. Zlotnik, Y. Chen, I. Z. Kiss, H. A. Tanaka, and J. S. Li, "Optimal waveform for fast entrainment of weakly forced nonlinear oscillators," Phys. Rev. Lett. **111**(2), 024102 (2013).